

# Unified description of correlations in double quantum dots

Vyacheslavs Kashcheyevs,<sup>1,\*</sup> Avraham Schiller,<sup>2</sup> Amnon Aharony,<sup>3</sup> and Ora Entin-Wohlman<sup>3,4</sup>

<sup>1</sup>*School of Physics and Astronomy, Raymond and Beverly Sackler Faculty of Exact Sciences,  
Tel Aviv University, Tel Aviv 69978, Israel*

<sup>2</sup>*Racah Institute of Physics, The Hebrew University, Jerusalem 91904, Israel*

<sup>3</sup>*Department of Physics, Ben Gurion University, Beer Sheva 84105, Israel*

<sup>4</sup>*Albert Einstein Minerva Center for Theoretical Physics,  
Weizmann Institute of Science, Rehovot 76100, Israel*

The two-level model for a double quantum dot coupled to two leads, which is ubiquitously used to describe charge oscillations, transmission-phase lapses and correlation-induced resonances, is considered in its general form. The model features arbitrary tunnelling matrix elements among the two levels and the leads and between the levels themselves (including the effect of Aharonov-Bohm fluxes), as well as inter-level repulsive interactions. We show that this model is exactly mapped onto a generalized Anderson model of a single impurity, where the electrons acquire a pseudo-spin degree of freedom, which is conserved by the tunnelling but not within the dot. Focusing on the local-moment regime where the dot is singly occupied, we show that the effective low-energy Hamiltonian is that of the anisotropic Kondo model in the presence of a tilted magnetic field. For moderate values of the (renormalized) field, the Bethe *ansatz* solution of the isotropic Kondo model allows us to derive accurate expressions for the dot occupation numbers, and henceforth its zero-temperature transmission. Our results are in excellent agreement with those obtained from the Bethe *ansatz* for the isotropic Anderson model, and with the functional and numerical renormalization-group calculations of Meden and Marquardt [Phys. Rev. Lett. **96**, 146801 (2006)], which are valid for the general anisotropic case. In addition we present highly accurate estimates for the validity of the Schrieffer-Wolff transformation (which maps the Anderson Hamiltonian onto the low-energy Kondo model) at both the high- and low-magnetic field limits. Perhaps most importantly, we provide a single coherent picture for the host of phenomena to which this model has been applied.

PACS numbers: 73.63.Kv, 72.15.Qm, 75.20.Hr, 73.23.Hk

Keywords: quantum dots, multi-level transport, Kondo effect, Bethe *ansatz*, singular value decomposition

## I. INTRODUCTION

The ongoing technological progress in the fabrication and control of nanoscale electronic circuits, such as quantum dots, has stimulated detailed studies of various quantum-impurity models, where a few local degrees of freedom are coupled to a continuum. Of particular interest are models with experimentally verifiable universal properties. One of the best studied examples is the Anderson single impurity model,<sup>1</sup> which describes successfully electronic correlations in small quantum dots.<sup>2,3</sup> The experimental control of most of the parameters of this model, e.g., the impurity energy level position or the level broadening due to hybridization with the continuum, allows for detailed investigations<sup>4,5</sup> of the universal low-temperature behavior of the Anderson model.

In this paper we study the low-energy behavior of a generic model, depicted in Fig. 1a, which pertains either to a single two-level quantum dot or to a double quantum dot where each dot harbors only a single level. The spin degeneracy of the electrons is assumed to be lifted by an external magnetic field. Several variants of this model have been studied intensely in recent years, in conjunction with a plethora of phenomena, such as many-body resonances in the spectral density,<sup>6</sup> phase lapses in the transmission phase,<sup>7,8</sup> charge oscillations,<sup>9,10</sup> and correlation-induced resonances in the conductance.<sup>11,12</sup> Albeit being described by the same model, no clear link-

age has been established between these seemingly different effects. The reason is in part due to the large number of model parameters involved, which so far obscured a clear physical picture. While some exact statements can be made, these are restricted to certain solvable limits,<sup>6</sup> and are apparently nongeneric.<sup>11</sup> Here we construct a framework which encompasses all parameter regimes of the model, and enables a unified description of the various phenomena alluded to above, exposing their common physical origin. For the most interesting regime of strong fluctuations between the two levels, we are able to give: (i) explicit analytical conditions for the occurrence of transmission phase lapses; (ii) an explanation of the population inversion and the charge oscillations<sup>9,10,13</sup> (including a Kondo enhancement of the latter); (iii) a complete account of the correlation-induced resonances<sup>11</sup> as a disguised Kondo phenomenon.

After introducing the details of the double-dot Hamiltonian in Sec. II A, we begin our analysis by constructing a linear transformation of the dot operators, *and* a simultaneous (generally different) linear transformation of the lead operators, such that the  $2 \times 2$  tunnelling matrix between the two levels on the dot and the leads becomes diagonal (with generally different eigenvalues). As a result, the electrons acquire a pseudo-spin degree of freedom which is conserved upon tunnelling between the dot and the continuum, as shown schematically in Fig. 1b. Concomitantly, the transformation generates a local Zee-

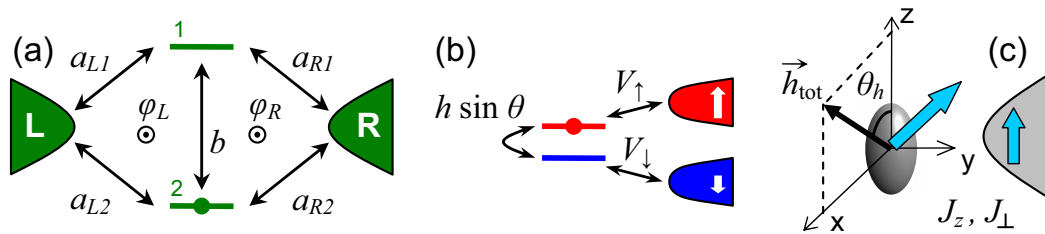


FIG. 1: A schematic representation of the double-dot system, along with its reduction in the local-moment regime to an effective Kondo model with a tilted magnetic field. (a) The model system: two localized levels coupled by tunnelling matrix elements to one another and to two separate leads. A constant magnetic flux induces phase factors on those elements. Spinless electrons residing on the two levels experience a repulsive interaction. (b) The mapping onto a spinful generalized Anderson model, with a tilted magnetic field and different tunnelling elements for spin-up and spin-down electrons. (c) The low-energy behavior of the generalized Anderson model is mapped onto an anisotropic Kondo model with a tilted magnetic field,  $\vec{h}_{\text{tot}}$ .

man magnetic field. In this way the original double-dot model system is transformed into a generalized Anderson impurity model in the presence of a (generally tilted) external magnetic field. This first stage is detailed in Sec. II B and Appendix A.

We next analyze in Sec. III the low-energy properties of our generalized Anderson model. We confine ourselves to the local moment regime, in which there is a single electron on the impurity. The fluctuations of the pseudo-spin degree of freedom (which translate into charge fluctuations between the two localized levels in the original model) are determined by two competing effects: the polarizing effect of the local magnetic field, and the Kondo screening by the itinerant electrons. In order to quantitatively analyze this competition, we derive an effective low-energy Kondo Hamiltonian, using Haldane's scaling procedure,<sup>14</sup> together with the Schrieffer-Wolff<sup>15</sup> transformation and Anderson's poor man's scaling.<sup>16</sup> This portion of the derivation resembles recent studies of the Kondo effect in the presence of ferromagnetic leads,<sup>17</sup> although the physical context and implications are quite different.

As is mentioned above, the tunnelling between the impurity and the continuum in the generalized Anderson model is (pseudo) spin dependent. This asymmetry results in two important effects: (a) different renormalizations of the two local levels, which in turn generates an additional local magnetic field.<sup>17</sup> This field is not necessarily aligned with the original Zeeman field that is present in the generalized Anderson model. (b) An anisotropy of the exchange coupling between the conduction electrons and the local moment in the Kondo Hamiltonian. However, since the scaling equations for the anisotropic Kondo model<sup>16,18</sup> imply a flow towards the *isotropic* strong coupling fixed point, the low-energy behavior of the generalized Anderson model can be still described in terms of two competing energy scales, the Kondo temperature,  $T_K$ , and the renormalized magnetic field,  $h_{\text{tot}}$ . Our two-stage mapping, double-dot  $\Rightarrow$  generalized Anderson model  $\Rightarrow$  anisotropic Kondo model (see Fig. 1), allows us to obtain analytic expressions for the original model properties in terms of those of the Kondo

model. We derive in Sec. IV the occupation numbers on the two localized levels by employing the Bethe *ansatz* solution of the magnetization of a Kondo spin in a finite magnetic field.<sup>19,20</sup> This solution also results in a highly accurate expression for the conductance based upon the Friedel-Langreth sum rule.<sup>21</sup> Perhaps most importantly, it provides a single coherent picture for the host of phenomena to which our model has been applied.

Examples of explicit results stemming from our general analysis are presented in Sec. V. First, we consider the case in which the tunnelling is isotropic, being the same for spin-up and spin-down electrons. Then the model is exactly solvable by direct application of the Bethe *ansatz* to the Anderson Hamiltonian.<sup>20,22</sup> We solve the resulting equations<sup>22,23</sup> numerically and obtain the occupation numbers for arbitrary parameter values of the model, and in particular, for arbitrary values of the local Zeeman field. By comparing with the occupation numbers obtained in Sec. IV from the Kondo version of the model, we are able to test the accuracy of the Schrieffer-Wolff mapping onto the Kondo Hamiltonian. We find that this mapping yields extremely precise results over the entire local-moment regime. This exactly solvable example has another virtue. It clearly demonstrates the competition between the Kondo screening of the local spin, which is governed by  $T_K$ , and the polarizing effect of the local field  $h_{\text{tot}}$ . This competition is reflected in the charging process of the quantum dot described by the original Hamiltonian. We next proceed to apply our general method to the features for which the anisotropy in the tunnelling is relevant, notably the transmission phase lapses and the correlation-induced resonances.<sup>11</sup> In particular, we derive analytical expressions for the occupation numbers and the conductance employing the mapping onto the Kondo Hamiltonian. These analytical expressions give results which are in a very good agreement with the data presented by Meden and Marquardt,<sup>11</sup> which was obtained by the functional and numerical renormalization-group methods applied to the original model.

As our treatment makes extensive usage of the exact Bethe *ansatz* solutions for the impurity magnetization in the isotropic Kondo and Anderson models with a finite

magnetic field, all relevant details of the solutions are concisely gathered for convenience in Appendix B.

## II. THE DOUBLE-DOT SYSTEM AS A GENERALIZED ANDERSON MODEL

### A. The model

We consider spinless electrons in a system of two distinct energy levels (a ‘quantum dot’), labelled  $i = 1, 2$ , which are connected by tunnelling to two leads, labelled  $\alpha = L, R$ . This quantum dot is penetrated by a (constant) magnetic flux. The total Hamiltonian of the system reads

$$\mathcal{H} = \mathcal{H}_l + \mathcal{H}_d + \mathcal{H}_{ld}, \quad (1)$$

in which  $\mathcal{H}_l$  is the Hamiltonian of the leads,  $\mathcal{H}_d$  is the Hamiltonian of the isolated dot, and  $\mathcal{H}_{ld}$  describes the coupling between the dot and the leads. The system is portrayed schematically in Fig. 1a.

Each of the leads is modelled by a continuum of noninteracting energy levels lying within a band of width  $2D$ , with a constant density of states  $\rho$ .<sup>24</sup> The corresponding Hamiltonian is given by

$$\mathcal{H}_l = \sum_{k\alpha} \varepsilon_k c_{k\alpha}^\dagger c_{k\alpha}, \quad (2)$$

where  $c_{k\alpha}^\dagger$  ( $c_{k\alpha}$ ) creates (annihilates) an electron of wave vector  $k$  on lead  $\alpha$ . The two leads are connected to two external reservoirs, held at the same temperature  $T$  and having different chemical potentials,  $\mu_L$  and  $\mu_R$ , respectively. We take the limit  $\mu_L \rightarrow \mu_R = 0$  in considering equilibrium properties and the linear conductance.

The isolated dot is described by the Hamiltonian

$$\mathcal{H}_d = \begin{bmatrix} d_1^\dagger & d_2^\dagger \end{bmatrix} \cdot \hat{\mathcal{E}}_d \cdot \begin{bmatrix} d_1 \\ d_2 \end{bmatrix} + U n_1 n_2, \quad (3)$$

where

$$\hat{\mathcal{E}}_d = \frac{1}{2} \begin{bmatrix} 2\epsilon_0 + \Delta & b e^{i(\varphi_L - \varphi_R)/2} \\ b e^{-i(\varphi_L - \varphi_R)/2} & 2\epsilon_0 - \Delta \end{bmatrix}. \quad (4)$$

Here,  $d_i^\dagger$  ( $d_i$ ) creates (annihilates) an electron on the  $i$ th level,  $n_i \equiv d_i^\dagger d_i$  are the occupation-number operators (representing the local charge),  $U > 0$  denotes the

Coulomb repulsion between electrons that occupy the two levels,  $\epsilon_0 \pm \Delta/2$  are the (single-particle) energies on the levels, and  $b/2$  is the amplitude for tunnelling between them. The phases  $\varphi_L$  and  $\varphi_R$ , respectively, represent the Aharonov-Bohm fluxes (measured in units of the flux quantum  $2\pi\hbar c/e$ ) in the left and in the right hopping loops, such that the total flux in the two loops is  $\varphi \equiv \varphi_L + \varphi_R$  [see Fig. 1a].

Gauge invariance grants us the freedom to distribute the Aharonov-Bohm phases among the inter-dot coupling  $b$  and the couplings between the dot levels and the leads. With the convention of Eq. (4), the coupling between the quantum dot and the leads is described by the Hamiltonian

$$\mathcal{H}_{ld} = \sum_k \begin{bmatrix} c_{kL}^\dagger & c_{kR}^\dagger \end{bmatrix} \cdot \hat{A} \cdot \begin{bmatrix} d_1 \\ d_2 \end{bmatrix} + \text{H.c.}, \quad (5)$$

where

$$\hat{A} = \begin{bmatrix} a_{L1} e^{i\varphi/2} & a_{L2} \\ a_{R1} & a_{R2} e^{i\varphi/2} \end{bmatrix}, \quad \varphi = \varphi_L + \varphi_R. \quad (6)$$

Here the real (possibly negative) coefficients  $a_{\alpha i}$  are the tunnelling amplitudes for transferring an electron from the level  $i$  to lead  $\alpha$ . Note that the Hamiltonian depends solely on the total Aharonov-Bohm flux  $\varphi$  when the interdot coupling  $b$  vanishes. Also, the tunnelling matrix  $\hat{A}$  is assumed to be independent of the wave vector  $k$ . This assumption considerably simplifies the analysis while keeping the main physical picture intact.

### B. Mapping onto a generalized Anderson model

The analysis of the model defined in Sec. II A employs an *exact* mapping of the Hamiltonian of Eq. (1) onto a generalized Anderson Hamiltonian, which pertains to a single-level quantum dot, coupled to a spin-degenerate band of conduction electrons. We show in Appendix A that the model depicted in Fig. 1a is fully described by the Hamiltonian

$$\mathcal{H} = \sum_{k,\sigma} \varepsilon_k c_{k\sigma}^\dagger c_{k\sigma} + \sum_{\sigma} \left( \epsilon_0 - \sigma \frac{\hbar}{2} \cos \theta \right) n_{\sigma} - (d_{\uparrow}^\dagger d_{\downarrow} + d_{\downarrow}^\dagger d_{\uparrow}) \frac{\hbar}{2} \sin \theta + U n_{\uparrow} n_{\downarrow} + \sum_{k,\sigma} V_{\sigma} \left( c_{k\sigma}^\dagger d_{\sigma} + \text{H.c.} \right), \quad (7)$$

schematically sketched Fig. 1b, which generalizes the original Anderson model<sup>1</sup> in two aspects. Firstly, it al-

lows for spin-dependent coupling between the dot and

the conduction band. A similar variant of the Anderson model has recently attracted much theoretical and experimental attention in connection with the Kondo effect for ferromagnetic leads.<sup>17,25,26,27,28</sup> Secondly, it allows for a Zeeman field whose direction is inclined with respect to the “anisotropy” axis  $z$ . For spin-independent tunnelling, one can easily realign the field along the  $z$  axis by a simple rotation of the different operators about the  $y$  axis. This is no longer the case once  $V_\uparrow \neq V_\downarrow$ , which precludes the use of some of the exact results available for the Anderson model. As we show below, the main effect of spin-dependent tunnelling is to modify the effective field seen by electrons on the dot, by renormalizing its  $z$ -component.

The derivation of Eq. (7) is accomplished by a transformation known as the singular-value decomposition,<sup>29</sup> which allows one to express the tunnelling matrix  $\hat{A}$  in the form

$$\hat{A} = R_l^\dagger \cdot \begin{bmatrix} V_\uparrow & 0 \\ 0 & V_\downarrow \end{bmatrix} \cdot R_d. \quad (8)$$

Here  $R_l$  and  $R_d$  are unitary  $2 \times 2$  matrices, which are used to independently rotate the lead and the dot operators according to

$$\begin{bmatrix} d_\uparrow \\ d_\downarrow \end{bmatrix} \equiv R_d \cdot \begin{bmatrix} d_1 \\ d_2 \end{bmatrix}, \quad \begin{bmatrix} c_{k\uparrow} \\ c_{k\downarrow} \end{bmatrix} \equiv R_l \cdot \begin{bmatrix} c_{kL} \\ c_{kR} \end{bmatrix}. \quad (9)$$

To make contact with the conventional Anderson impurity model, we have labelled the linear combinations of the original operators [defined through Eqs. (9)] by the “spin” index  $\sigma = \uparrow (+1)$  and  $\sigma = \downarrow (-1)$ .

The transformation (9) generalizes the one in which the *same* rotation  $R$  is applied to both the dot and the lead operators. It is needed in the present, more general, case since the matrix  $\hat{A}$  generically lacks an orthogonal basis of eigenvectors. The matrices  $R_d$  and  $R_l$  can always be chosen uniquely (up to a common overall phase) such that<sup>30</sup> (a) the tunnelling between the dot and the continuum is diagonal in the spin basis (so that the tunnelling conserves the spin); (b) the amplitudes  $V_\uparrow \geq V_\downarrow \geq 0$  are real; and (c) the part of the Hamiltonian of Eq. (7) pertaining to the dot has only real matrix elements with  $h \sin \theta \geq 0$ . The explicit expressions for the rotation matrices  $R_d$  and  $R_l$  as well as for the model parameters appearing in Eq. (7) in terms of those of the original Hamiltonian are given in Appendix A.

It should be emphasized that partial transformations involving only one rotation matrix, either  $R_d$  or  $R_l$ , have previously been applied in this context (see, e.g., Refs. 6 and 31). However, excluding special limits, both  $R_d$  and  $R_l$  are required to expose the formal connection to the Anderson model. A first step in this direction was recently taken by Golosov and Gefen,<sup>8</sup> yet only on a restricted manifold for the tunnelling amplitudes  $a_{\alpha i}$ . In the following section we discuss in detail the low-energy physics of the Hamiltonian of Eq. (7), focusing on the local-moment regime. Explicit results for the conduc-

tance and the occupations of the levels are then presented in Secs. IV and V.

### III. THE LOCAL-MOMENT REGIME

There are two limits where the model of Eq. (1) has an exact solution:<sup>6</sup> (i) when the spin-down state is decoupled in Eq. (7), i.e., when  $V_\downarrow = h \sin \theta = 0$ ; (ii) when the coupling is isotropic, i.e.,  $V_\uparrow = V_\downarrow$ . In the former case,  $n_\downarrow$  is conserved. The Hilbert space separates then into two disconnected sectors with  $n_\downarrow = 0$  and  $n_\downarrow = 1$ . Within each sector, the Hamiltonian can be diagonalized independently as a single-particle problem. In the latter case, one can always align the magnetic field  $h$  along the  $z$  axis by a simple rotation of the different operators about the  $y$  axis. The model of Eq. (7) reduces then to a conventional Anderson model in a magnetic field, for which an exact Bethe *ansatz* solution is available.<sup>20</sup> (This special case will be analyzed in great detail in Sec. V A.)

In terms of the model parameters appearing in the original Hamiltonian, the condition  $V_\downarrow = 0$  corresponds to

$$|a_{L1}a_{R2}| = |a_{R1}a_{L2}|, \quad \text{and} \quad \varphi = \beta \bmod 2\pi, \quad (10)$$

whereas  $V_\uparrow = V_\downarrow = V$  corresponds to

$$|a_{L1}| = |a_{R2}|, \quad |a_{L2}| = |a_{R1}|, \quad \text{and} \quad \varphi = (\pi + \beta) \bmod 2\pi. \quad (11)$$

Here

$$\beta = \begin{cases} 0 & \text{if } a_{L1}a_{L2}a_{R1}a_{R2} > 0 \\ \pi & \text{if } a_{L1}a_{L2}a_{R1}a_{R2} < 0 \end{cases} \quad (12)$$

records the combined signs of the four coefficients  $a_{\alpha i}$ .<sup>32</sup>

Excluding the two cases mentioned above, no exact solutions to the Hamiltonian of Eq. (1) are known. Nevertheless, we shall argue below that the model displays generic low-energy physics in the “local-moment” regime, corresponding to the Kondo effect in a finite magnetic field. To this end we focus hereafter on  $\Gamma_\uparrow, \Gamma_\downarrow, h \ll -\epsilon_0, U + \epsilon_0$ , and derive an effective low-energy Hamiltonian for general couplings. Here  $\Gamma_\sigma = \pi \rho V_\sigma^2$  is half the tunnelling rate between the spin state  $\sigma$  and the leads.

#### A. Effective low-energy Hamiltonian

As is mentioned above, when  $V_\uparrow = V_\downarrow$  one is left with a conventional Kondo effect in the presence of a finite magnetic field. Asymmetry in the couplings,  $V_\uparrow \neq V_\downarrow$ , changes this situation in three aspects. Firstly, the effective magnetic field seen by electrons on the dot is modified, acquiring a renormalized  $z$ -component. Secondly, the elimination of the charge fluctuations by means of a Schrieffer-Wolff transformation,<sup>15</sup> results in an anisotropic spin-exchange interaction. Thirdly, a new interaction term is produced, coupling the spin and the

charge. Similar aspects have been previously discussed in the context of the Kondo effect in the presence of ferromagnetic leads,<sup>17</sup> where the source of the asymmetry is the inequivalent density of states for conduction electrons with opposite spin.<sup>28</sup> Below we elaborate on the emergence of these features in the present case.

Before turning to a detailed derivation of the effective low-energy Hamiltonian, we briefly comment on the physical origin of the modified magnetic field. As is well known, the coupling to the continuum renormalizes the bare energy levels of the dot. For  $\Gamma_\uparrow, \Gamma_\downarrow, h \ll -\epsilon_0, U + \epsilon_0$ , these renormalizations can be accurately estimated using second-order perturbation theory in  $V_\sigma$ . For  $V_\uparrow \neq V_\downarrow$ , each of the bare levels  $\epsilon_\sigma = \epsilon_0 - \frac{1}{2}\sigma h \cos \theta$  is shifted by a different amount, which acts in effect as an excess magnetic field. Explicitly, for  $T = 0$  and  $D \gg |\epsilon_0|, U$  one obtains<sup>13,17</sup>

$$\Delta h_z = \frac{\Gamma_\uparrow - \Gamma_\downarrow}{\pi} \ln \frac{\epsilon_0 + U}{|\epsilon_0|}. \quad (13)$$

As  $\epsilon_0$  is swept across  $-U/2$ ,  $\Delta h_z \propto \Gamma_\uparrow - \Gamma_\downarrow$  changes sign. Had  $|\Gamma_\uparrow - \Gamma_\downarrow|$  exceeded  $h$  this would have dictated a sign-reversal of the  $z$ -component of the combined field as  $\epsilon_0$  is tuned across the Coulomb-blockade valley. As originally noted by Silvestrov and Imry,<sup>13</sup> this simple but insightful observation underlies the population inversion discussed in Refs.9,10 and 13 for a singly occupied dot. We shall return to this important point in greater detail later on.

A systematic derivation of the effective low-energy Hamiltonian for  $\Gamma_\uparrow, \Gamma_\downarrow, h \ll -\epsilon_0, U + \epsilon_0$  involves the combination of Anderson's poor-man's scaling<sup>16</sup> and the Schrieffer-Wolff transformation.<sup>15</sup> For  $|\epsilon_0| \sim U + \epsilon_0$ , the elimination of high-energy excitations proceeds in three steps. First Haldane's perturbative scaling approach<sup>14</sup> is applied to progressively reduce the bandwidth from its bare value  $D$  down to  $D_{\text{SW}} \sim |\epsilon_0| \sim U + \epsilon_0$ . Next a Schrieffer-Wolff transformation is carried out to eliminate charge fluctuations on the dot. At the conclusion of this second step one is left with a generalized Kondo Hamiltonian [Eq. (16) below], featuring an anisotropic spin-exchange interaction and an additional interaction term that couples spin and charge. The Kondo Hamiltonian also includes a finite magnetic field whose direction is inclined with respect to the anisotropy axis  $z$ . In the third and final stage, the Kondo Hamiltonian is treated using Anderson's poor-man's scaling<sup>16</sup> to expose its low-energy physics.

The above procedure is further complicated in the case where  $|\epsilon_0|$  and  $U + \epsilon_0$  are well separated in energy. This situation requires two distinct Schrieffer-Wolff transformations: one at  $D_{\text{SW}}^{\text{up}} \sim \max\{|\epsilon_0|, U + \epsilon_0\}$  and the other at  $D_{\text{SW}}^{\text{down}} \sim \min\{|\epsilon_0|, U + \epsilon_0\}$ . Reduction of the bandwidth from  $D_{\text{SW}}^{\text{up}}$  to  $D_{\text{SW}}^{\text{down}}$  is accomplished using yet another (third) segment of the perturbative scaling. It turns out that all possible orderings of  $|\epsilon_0|$  and  $U + \epsilon_0$  produce the same Kondo Hamiltonian, provided that  $\Gamma_\uparrow, \Gamma_\downarrow$  and  $h$  are sufficiently small. To keep the discussion as concise as possible, we therefore restrict the presentation

to the case  $|\epsilon_0| \sim U + \epsilon_0$ .

Consider first the energy window between  $D$  and  $D_{\text{SW}}$ , which is treated using Haldane's perturbative scaling.<sup>14</sup> Suppose that the bandwidth has already been lowered from its initial value  $D$  to some value  $D' = De^{-l}$  with  $0 < l < \ln(D/D_{\text{SW}})$ . Further reducing the bandwidth to  $D'(1 - \delta l)$  produces a renormalization of each of the energies  $\epsilon_\uparrow, \epsilon_\downarrow$ , and  $U$ . Specifically, the  $z$ -component of the magnetic field,  $h_z \equiv \epsilon_\downarrow - \epsilon_\uparrow$ , is found to obey the scaling equation

$$\frac{dh_z}{dl} = \frac{\Gamma_\uparrow - \Gamma_\downarrow}{\pi} \left[ \frac{1}{1 - e^l \epsilon_0/D} - \frac{1}{1 + e^l (U + \epsilon_0)/D} \right]. \quad (14)$$

Here we have retained  $\epsilon_0$  and  $U + \epsilon_0$  in the denominators, omitting corrections which are higher-order in  $\Gamma_\uparrow, \Gamma_\downarrow$ , and  $h$  (these include also the small renormalizations of  $\epsilon_\sigma$  and  $U$  that are accumulated in the course of the scaling). The  $x$ -component of the field,  $h_x = h \sin \theta$ , remains unchanged throughout the procedure. Upon reaching  $D' = D_{\text{SW}}$ , the renormalized field  $h_z$  becomes

$$h_z^* = h \cos \theta + \frac{\Gamma_\uparrow - \Gamma_\downarrow}{\pi} \ln \frac{D_{\text{SW}} + U + \epsilon_0}{D_{\text{SW}} - \epsilon_0}, \quad (15)$$

where we have assumed  $D \gg |\epsilon_0|, U$ .

Once the scale  $D_{\text{SW}}$  is reached, charge fluctuations on the dot are eliminated via a Schrieffer-Wolff transformation,<sup>15</sup> which generates among other terms also further renormalizations of  $\epsilon_\sigma$ . Neglecting  $h$  in the course of the transformation, one arrives at the following Kondo-type Hamiltonian,

$$\begin{aligned} \mathcal{H}_K = & \sum_{k,\sigma} \epsilon_k c_{k\sigma}^\dagger c_{k\sigma} + J_\perp (S_x s_x + S_y s_y) + J_z S_z s_z \\ & + v_{\text{sc}} S^z \sum_{k,k',\sigma} :c_{k\sigma}^\dagger c_{k'\sigma}: + \sum_{k,k',\sigma} (v_+ + \sigma v_-) :c_{k\sigma}^\dagger c_{k'\sigma}: \\ & - \tilde{h}_z S_z - \tilde{h}_x S_x. \end{aligned} \quad (16)$$

Here we have represented the local moment on the dot by the spin- $\frac{1}{2}$  operator

$$\vec{S} = \frac{1}{2} \sum_{\sigma,\sigma'} \vec{\tau}_{\sigma\sigma'} d_\sigma^\dagger d_{\sigma'} \quad (17)$$

( $\vec{\tau}$  being the Pauli matrices), while

$$\vec{s} = \frac{1}{2} \sum_{k,k'} \sum_{\sigma,\sigma'} \vec{\tau}_{\sigma\sigma'} c_{k\sigma}^\dagger c_{k'\sigma'} \quad (18)$$

are the local conduction-electron spin densities. The symbol  $:c_{k\sigma}^\dagger c_{k'\sigma}: = c_{k\sigma}^\dagger c_{k'\sigma} - \delta_{k,k'} \theta(-\epsilon_k)$  stands for normal ordering with respect to the filled Fermi sea. The various couplings that appear in Eq. (16) are given by the explicit expressions

$$\rho J_\perp = \frac{2\sqrt{\Gamma_\uparrow \Gamma_\downarrow}}{\pi} \left( \frac{1}{|\epsilon_0|} + \frac{1}{U + \epsilon_0} \right), \quad (19)$$

$$\rho J_z = \frac{\Gamma_\uparrow + \Gamma_\downarrow}{\pi} \left( \frac{1}{|\epsilon_0|} + \frac{1}{U + \epsilon_0} \right), \quad (20)$$

$$\rho v_{sc} = \frac{\Gamma_\uparrow - \Gamma_\downarrow}{4\pi} \left( \frac{1}{|\epsilon_0|} + \frac{1}{U + \epsilon_0} \right), \quad (21)$$

$$\rho v_\pm = \frac{\Gamma_\uparrow \pm \Gamma_\downarrow}{4\pi} \left( \frac{1}{|\epsilon_0|} - \frac{1}{U + \epsilon_0} \right), \quad (22)$$

$$\tilde{h}_z = h \cos \theta + \frac{\Gamma_\uparrow - \Gamma_\downarrow}{\pi} \ln \frac{U + \epsilon_0}{|\epsilon_0|}, \quad (23)$$

and

$$\tilde{h}_x = h \sin \theta. \quad (24)$$

Equations (19)–(24) are correct to leading order in  $\Gamma_\uparrow$ ,  $\Gamma_\downarrow$ , and  $h$ , in accordance with the inequality  $\Gamma_\uparrow, \Gamma_\downarrow, h \ll |\epsilon_0|, U + \epsilon_0$ . In fact, additional terms are generated in Eq. (16) when  $h$  is kept in the course of the Schrieffer-Wolff transformation. However, the neglected terms are smaller than the ones retained by a factor of  $h/\min\{|\epsilon_0|, U + \epsilon_0\} \ll 1$ , and are not expected to alter the low-energy physics in any significant way. We also note that  $\tilde{h}_z$  accurately reproduces the second-order correction to  $h_z$  detailed in Eq. (13). As emphasized above, the same effective Hamiltonian is obtained when  $|\epsilon_0|$  and  $U + \epsilon_0$  are well separated in energy, although the derivation is notably more cumbersome. In unifying the different possible orderings of  $|\epsilon_0|$  and  $U + \epsilon_0$ , the effective bandwidth in Eq. (16) must be taken to be  $D_0 \sim \min\{|\epsilon_0|, U + \epsilon_0\}$ .

### B. Reduction to the Kondo effect in a finite magnetic field

In addition to spin-exchange anisotropy and a tilted magnetic field, the Hamiltonian of Eq. (16) contains a new interaction term,  $v_{sc}$ , which couples spin and charge. It also includes spin-dependent potential scattering, represented by the term  $v_-$  above. As is well known, spin-exchange anisotropy is irrelevant for the conventional spin- $\frac{1}{2}$  single-channel Kondo problem. As long as one lies within the confines of the antiferromagnetic domain, the system flows to the same strong-coupling fixed point no matter how large the exchange anisotropy is.  $SU(2)$  spin symmetry is thus restored at low energies. A finite magnetic field  $h$  cuts off the flow to isotropic couplings, as does the temperature  $T$ . However, the residual anisotropy is negligibly small if  $h$ ,  $T$  and the bare couplings are small. That is, low-temperature thermodynamic and dynamic quantities follow a single generic dependence on  $T/T_K$  and  $h/T_K$ , where  $T_K$  is the Kondo

temperature. All relevant information on the bare spin-exchange anisotropy is contained for weak couplings in the microscopic form of  $T_K$ .

The above picture is insensitive to the presence of weak potential scattering, which only slightly modifies the conduction-electron phase shift at the Fermi energy. As we show below, neither is it sensitive to the presence of the weak couplings  $v_{sc}$  and  $v_-$  in Eq. (16). This observation is central to our discussion, as it enables a very accurate and complete description of the low-energy physics of  $\mathcal{H}_K$  in terms of the conventional Kondo model in a finite magnetic field. Given the Kondo temperature  $T_K$  and the direction and magnitude of the renormalized field pertaining to Eq. (16), physical observables can be extracted from the exact Bethe *ansatz* solution of the conventional Kondo model. In this manner, one can accurately compute the conductance and the occupation of the levels, as demonstrated in Secs. IV and V.

To establish this important point, we apply poor-man's scaling<sup>16</sup> to the Hamiltonian of Eq. (16). Of the different couplings that appear in  $\mathcal{H}_K$ , only  $J_z$ ,  $J_\perp$ , and  $\tilde{h}_z$  are renormalized at second order. Converting to the dimensionless exchange couplings  $\tilde{J}_z = \rho J_z$  and  $\tilde{J}_\perp = \rho J_\perp$ , these are found to obey the standard scaling equations<sup>16,18</sup>

$$\frac{d\tilde{J}_z}{dl} = \tilde{J}_\perp^2, \quad (25)$$

$$\frac{d\tilde{J}_\perp}{dl} = \tilde{J}_z \tilde{J}_\perp, \quad (26)$$

independent of  $v_{sc}$  and  $v_\pm$ . Indeed, the couplings  $v_{sc}$  and  $v_\pm$  do not affect the scaling trajectories in any way, other than through a small renormalization to  $\tilde{h}_z$ :

$$\frac{d\tilde{h}_z}{dl} = D_0 e^{-l} \left( \tilde{J}_z \tilde{v}_- + 2\tilde{v}_{sc} \tilde{v}_+ \right) 8 \ln 2. \quad (27)$$

Here  $\tilde{v}_\mu$  are the dimensionless couplings  $\rho v_\mu$  ( $\mu = sc, \pm$ ), and  $l$  equals  $\ln(D_0/D')$  with  $D'$  the running bandwidth.

As stated above, the scaling equations (25)–(26) are identical to those obtained for the conventional anisotropic Kondo model. Hence, the Kondo couplings flow toward strong coupling along the same scaling trajectories and with the same Kondo temperature as in the absence of  $v_{sc}$  and  $v_\pm$ . Straightforward integration of Eqs. (25)–(26) yields

$$T_K = D_0 \exp \left( -\frac{1}{\rho \xi} \tanh^{-1} \frac{\xi}{J_z} \right) \quad (28)$$

with  $\xi = \sqrt{J_z^2 - J_\perp^2}$ . Here we have exploited the hierarchy  $J_z \geq J_\perp > 0$  in deriving Eq. (28). In terms of the original model parameters appearing in Eq. (7), Eq. (28) takes the form

$$T_K = D_0 \exp \left[ \frac{\pi \epsilon_0 (U + \epsilon_0)}{2U(\Gamma_\uparrow - \Gamma_\downarrow)} \ln \frac{\Gamma_\uparrow}{\Gamma_\downarrow} \right]. \quad (29)$$

Equation (29) was obtained within second-order scaling, which is known to overestimate the pre-exponential factor that enters  $T_K$ . We shall not seek an improved expression for  $T_K$  encompassing all parameter regimes of Eq. (7). More accurate expressions will be given for the particular cases of interest, see Sec. V below. Much of our discussion will not depend, though, on the precise form of  $T_K$ . We shall only assume it to be sufficiently small such that the renormalized exchange couplings can be regarded isotropic starting at energies well above  $T_K$ .

The other competing scale which enters the low-energy physics is the fully renormalized magnetic field:  $\vec{h}_{\text{tot}} = h_{\text{tot}}^x \hat{x} + h_{\text{tot}}^z \hat{z}$ . While the transverse field  $h_{\text{tot}}^x$  remains given by  $h \sin \theta$ , the longitudinal field  $h_{\text{tot}}^z$  is obtained by integration of Eq. (27), subject to the initial condition of Eq. (23). Since the running coupling  $\tilde{J}_z$  is a slowly varying function of  $l$  in the range where Eqs. (25)–(27) apply, it can be replaced for all practical purposes by its bare value in Eq. (27). Straightforward integration of Eq. (27) then yields

$$h_{\text{tot}}^z = h \cos \theta + \frac{\Gamma_{\uparrow} - \Gamma_{\downarrow}}{\pi} \ln \frac{U + \epsilon_0}{|\epsilon_0|} + 3 \ln(2) D_0 \frac{\Gamma_{\uparrow}^2 - \Gamma_{\downarrow}^2}{\pi^2} \times \frac{U(U + 2\epsilon_0)}{(U + \epsilon_0)^2 \epsilon_0^2}, \quad (30)$$

where we have used Eqs. (20)–(22) for  $J_z$ ,  $v_{\text{sc}}$ , and  $v_{\pm}$ . Note that the third term on the right-hand side of Eq. (30) is generally much smaller than the first two terms, and can typically be neglected.

To conclude this section, we have shown that the Hamiltonian of Eq. (7), and thus that of Eq. (1), is equivalent at sufficiently low temperature and fields to the ordinary *isotropic* Kondo model with a tilted magnetic field, provided that  $\Gamma_{\uparrow}, \Gamma_{\downarrow} \ll |\epsilon_0|, U + \epsilon_0$ . The relevant Kondo temperature is approximately given by Eq. (29), while the components of  $\vec{h}_{\text{tot}} = h_{\text{tot}}^x \hat{x} + h_{\text{tot}}^z \hat{z}$  are given by  $h_{\text{tot}}^x = h \sin \theta$  and Eq. (30).

#### IV. PHYSICAL OBSERVABLES

Having established the intimate connection between the generalized Anderson Hamiltonian, Eq. (7), and the standard Kondo model with a tilted magnetic field, we now employ well-known results of the latter model in order to obtain a unified picture for the conductance and the occupation of the levels of our original model, Eq. (1). The analysis extends over a rather broad range of parameters. For example, when  $U + 2\epsilon_0 = 0$ , then the sole requirement for the applicability of our results is for  $\sqrt{\Delta^2 + b^2}$  to be small. The tunnelling matrix  $\hat{A}$  can be practically arbitrary as long as the system lies deep in the local-moment regime. The further one departs from the middle of the Coulomb-blockade valley the more restrictive the condition on  $\hat{A}$  becomes in order for  $\vec{h}_{\text{tot}}$  to stay small. Still, our approach is applicable over a surprisingly broad range of parameters, as demonstrated below.

Unless stated otherwise, our discussion is restricted to zero temperature.

##### A. Conductance

At zero temperature, a local Fermi liquid is formed in the Kondo model. Only elastic scattering takes place at the Fermi energy, characterized by the scattering phase shifts for the two appropriate conduction-electron modes. For a finite magnetic field  $h$  in the  $z$ -direction, single-particle scattering is diagonal in the spin index. The corresponding phase shifts,  $\delta_{\uparrow}(h)$  and  $\delta_{\downarrow}(h)$ , are given by the Friedel-Langreth sum rule,<sup>21,33</sup>  $\delta_{\sigma}(h) = \pi \langle n_{\sigma} \rangle$ , which when applied to the local-moment regime takes the form

$$\delta_{\sigma}(h) = \frac{\pi}{2} + \sigma \pi M(h). \quad (31)$$

Here  $M(h)$  is the spin magnetization, which reduces<sup>34</sup> in the scaling regime to a universal function of  $h/T_K$ ,

$$M(h) = M_K(h/T_K). \quad (32)$$

Thus, Eq. (31) becomes  $\delta_{\sigma}(h) = \pi/2 + \sigma \pi M_K(h/T_K)$ , where  $M_K(h/T_K)$  is given by Eq. (B1).

To apply these results to the problem at hand, one first needs to realign the tilted field along the  $z$  axis. This is achieved by a simple rotation of the different operators about the  $y$  axis. Writing the field  $\vec{h}_{\text{tot}}$  in the polar form

$$\begin{aligned} \vec{h}_{\text{tot}} &\equiv h_{\text{tot}} (\sin \theta_h \hat{x} + \cos \theta_h \hat{z}) \\ &\approx h \sin \theta \hat{x} + \left( h \cos \theta + \frac{\Gamma_{\uparrow} - \Gamma_{\downarrow}}{\pi} \ln \frac{U + \epsilon_0}{|\epsilon_0|} \right) \hat{z}, \end{aligned} \quad (33)$$

the lead and the dot operators are rotated according to

$$\begin{bmatrix} \tilde{c}_{k\uparrow} \\ \tilde{c}_{k\downarrow} \end{bmatrix} = R_h \cdot \begin{bmatrix} c_{k\uparrow} \\ c_{k\downarrow} \end{bmatrix} = R_h R_l \cdot \begin{bmatrix} c_{kL} \\ c_{kR} \end{bmatrix} \quad (34)$$

and

$$\begin{bmatrix} \tilde{d}_{\uparrow} \\ \tilde{d}_{\downarrow} \end{bmatrix} = R_h \cdot \begin{bmatrix} d_{\uparrow} \\ d_{\downarrow} \end{bmatrix} = R_h R_d \cdot \begin{bmatrix} d_1 \\ d_2 \end{bmatrix}, \quad (35)$$

with

$$R_h = e^{i(\theta_h/2)\tau_y} = \begin{bmatrix} \cos(\theta_h/2) & \sin(\theta_h/2) \\ -\sin(\theta_h/2) & \cos(\theta_h/2) \end{bmatrix}. \quad (36)$$

Here  $R_l$  and  $R_d$  are the unitary matrices used in Eq. (9) to independently rotate the lead and the dot operators. Note that since  $\sin \theta \geq 0$ , the range of  $\theta_h$  is  $\theta_h \in [0; \pi]$ .

The new dot and lead degrees of freedom have their spins aligned either parallel ( $\tilde{d}_{\uparrow}$  and  $\tilde{c}_{k\uparrow}$ ) or antiparallel ( $\tilde{d}_{\downarrow}$  and  $\tilde{c}_{k\downarrow}$ ) to the field  $\vec{h}_{\text{tot}}$ . In this basis the single-particle scattering matrix is diagonal,

$$\tilde{S} = - \begin{bmatrix} e^{i2\pi M_K(h_{\text{tot}}/T_K)} & 0 \\ 0 & e^{-i2\pi M_K(h_{\text{tot}}/T_K)} \end{bmatrix}. \quad (37)$$

The conversion back to the original basis set of left- and right-lead electrons is straightforward,

$$S = R_l^\dagger R_h^\dagger \tilde{S} R_h R_l \equiv \begin{bmatrix} r & t' \\ t & r' \end{bmatrix}, \quad (38)$$

providing us with the zero-temperature conductance  $G = (e^2/2\pi\hbar)|t|^2$ .

Equations (37) and (38) were derived employing the mapping of Eq. (1) onto an effective isotropic Kondo model with a tilted magnetic field, in the  $v_{\text{sc}}, v_{\pm} \rightarrow 0$  limit. Within this framework, Eqs. (37) and (38) are exact in the scaling regime,  $T_K/D_0 \ll 1$ . The extent to which these equations are indeed valid can be appreciated by considering the special case  $h \sin \theta = 0$ , for which there exists an exact (and independent) solution for the scattering matrix  $S$  in terms of the dot “magnetization”  $M = \langle n_\uparrow - n_\downarrow \rangle / 2$  [see Eq. (41) below]. That solution, which is based on the Friedel-Langreth sum rule<sup>21</sup> applied directly to a spin-conserving Anderson model, reproduces Eqs. (37) and (38) in the Kondo regime.

### 1. Zero Aharonov-Bohm fluxes

Of particular interest is the case where no Aharonov-Bohm fluxes are present, where further analytic progress can be made. For  $\varphi_L = \varphi_R = 0$ , the parameters that appear in the Hamiltonian of Eq. (1) are all real. Consequently, the rotation matrices  $R_d$  and  $R_l$  acquire the simplified forms given by Eqs. (A29) and (A32) (see Appendix A for details). Under these circumstances, the matrix product  $R_h R_l$  becomes  $\pm e^{i\tau_y(\theta_h + s_R \theta_l)/2} e^{i\pi\tau_z(1-s_R)/4}$ , and the elements of the scattering matrix [see Eq. (38)] are

$$\begin{aligned} t = t' &= -i \sin[2\pi M_K(h_{\text{tot}}/T_K)] \sin(\theta_l + s_R \theta_h), \\ r = (r')^* &= -\cos[2\pi M_K(h_{\text{tot}}/T_K)] \\ &\quad - i \sin[2\pi M_K(h_{\text{tot}}/T_K)] \cos(\theta_l + s_R \theta_h). \end{aligned} \quad (39)$$

Hence, the conductance is

$$G = \frac{e^2}{2\pi\hbar} \sin^2[2\pi M_K(h_{\text{tot}}/T_K)] \sin^2(\theta_l + s_R \theta_h), \quad (40)$$

where the sign  $s_R$  and angle  $\theta_l$  are given by Eqs. (A31) and (A23), respectively. All dependencies of the conductance on the original model parameters that enter Eq. (1) are combined in Eq. (40) into two variables alone,  $\theta_l + s_R \theta_h$  and the reduced field  $h_{\text{tot}}/T_K$ . In particular,  $\theta_l$  is determined exclusively by the tunnelling matrix  $\hat{A}$ , while  $s_R$  depends additionally on the two dot parameters  $\Delta$  and  $b$ .

The conditions for a phase lapse to occur are particularly transparent from Eq. (40). These lapses correspond to zeroes of  $t$ , and, in turn, of the conductance. There are two possibilities for  $G$  to vanish: either  $h_{\text{tot}}$  is zero, or  $\theta_l + s_R \theta_h$  equals an integer multiple of  $\pi$ . For example,

when the Hamiltonian of Eq. (7) is invariant under the particle-hole transformation  $d_\sigma \rightarrow d_\sigma^\dagger$  and  $c_{k\sigma} \rightarrow -c_{k\sigma}^\dagger$  (which happens to be the case whenever  $\sqrt{\Delta^2 + b^2} = 0$  and  $U + 2\epsilon_0 = 0$ ), then  $h_{\text{tot}}$  vanishes, and consequently the conductance vanishes as well. A detailed discussion of the ramifications of Eq. (40) is held in Sec. V B below.

### 2. Parallel-field configuration

For  $h \sin \theta = 0$ , spin is conserved by the Hamiltonian of Eq. (7). We refer to this case as the “parallel-field” configuration, since the magnetic field is aligned with the anisotropy axis  $z$ . For a parallel field, one can easily generalize the Friedel-Langreth sum rule<sup>21</sup> to the Hamiltonian of Eq. (7).<sup>25</sup> Apart from the need to consider each spin orientation separately, details of the derivation are identical to those for the ordinary Anderson model,<sup>21</sup> and so is the formal result for the  $T = 0$  scattering phase shift:  $\delta_\sigma = \pi \Delta N_\sigma$ , where  $\Delta N_\sigma$  is the number of displaced electrons in the spin channel  $\sigma$ . In the wide-band limit, adopted throughout our discussion,  $\Delta N_\sigma$  reduces to the occupancy of the corresponding dot level,  $\langle n_\sigma \rangle$ . The exact single-particle scattering matrix then becomes

$$S = e^{i\pi \langle n_\uparrow + n_\downarrow \rangle} R_l^\dagger \cdot \begin{bmatrix} e^{i2\pi M} & 0 \\ 0 & e^{-i2\pi M} \end{bmatrix} \cdot R_l, \quad (41)$$

where  $M = \langle n_\uparrow - n_\downarrow \rangle / 2$  is the dot “magnetization.”

Equation (41) is quite general. It covers all physical regimes of the dot, whether empty, singly occupied or doubly occupied, and extends to arbitrary fluxes  $\varphi_L$  and  $\varphi_R$ . Although formally exact, it does not specify how the dot “magnetization”  $M$  and the total dot occupancy  $\langle n_\uparrow + n_\downarrow \rangle$  relate to the microscopic model parameters that appear in Eq. (7). Such information requires an explicit solution for these quantities. In the Kondo regime considered above,  $\langle n_\uparrow + n_\downarrow \rangle$  is reduced to one and  $M$  is replaced by  $\pm M_K(h_{\text{tot}}/T_K)$ . Here the sign depends on whether the field  $\vec{h}_{\text{tot}}$  is parallel or antiparallel to the  $z$  axis (recall that  $h_{\text{tot}} \geq 0$  by definition). As a result, Eq. (41) reproduces Eqs. (37)–(38).

To carry out the rotation in Eq. (41), we rewrite it in the form

$$S = e^{i\pi \langle n_\uparrow + n_\downarrow \rangle} R_l^\dagger [\cos(2\pi M) + i \sin(2\pi M) \tau_z] R_l. \quad (42)$$

Using the general form of Eq. (A3) for the rotation matrix  $R_l$ , the single-particle scattering matrix is written as  $S = e^{i\pi \langle n_\uparrow + n_\downarrow \rangle} \tilde{S}$ , where

$$\begin{aligned} \tilde{S} &= \cos(2\pi M) + i \sin(2\pi M) \cos \theta_l \tau_z \\ &\quad + i \sin(2\pi M) \sin \theta_l [\cos \phi_l \tau_x + \sin \phi_l \tau_y]. \end{aligned} \quad (43)$$

The zero-temperature conductance,  $G = (e^2/2\pi\hbar)|t|^2$ , takes then the exact form

$$G = \frac{e^2}{2\pi\hbar} \sin^2(2\pi M) \sin^2 \theta_l. \quad (44)$$



Two distinct properties of the conductance are apparent from Eq. (44). Firstly,  $G$  is bounded by  $\sin^2 \theta_l$  times the conductance quantum unit  $e^2/2\pi\hbar$ . Unless  $\theta_l$  happens to equal  $\pm\pi/2$ , the maximal conductance is smaller than  $e^2/2\pi\hbar$ . Secondly,  $G$  vanishes for  $M = 0$  and is maximal for  $M = \pm 1/4$ . Consequently, when  $M$  is tuned from  $M \approx -1/2$  to  $M \approx 1/2$  by varying an appropriate control parameter (for example,  $\epsilon_0$  when  $\Gamma_\uparrow \gg \Gamma_\downarrow$ ), then  $G$  is peaked at the points where  $M = \pm 1/4$ . In the Kondo regime, when  $M \rightarrow \pm M_K(h_{\text{tot}}/T_K)$ , this condition is satisfied for  $h_{\text{tot}} \approx 2.4T_K$ . As we show in Sec. VB, this is the physical origin of the correlation-induced peaks reported by Meden and Marquardt.<sup>11</sup> Note that for a given fixed tunnelling matrix  $\hat{A}$  in the parallel-field configuration, the condition for a phase lapse to occur is simply for  $M$  to vanish.

### B. Occupation of the dot levels

Similar to the zero-temperature conductance, one can exploit exact results of the standard Kondo model to obtain the occupation of the levels at low temperatures and fields. Defining the two reduced density matrices

$$O_d = \begin{bmatrix} \langle d_1^\dagger d_1 \rangle & \langle d_2^\dagger d_1 \rangle \\ \langle d_1^\dagger d_2 \rangle & \langle d_2^\dagger d_2 \rangle \end{bmatrix} \quad (45)$$

and

$$\tilde{O}_d = \begin{bmatrix} \langle \tilde{d}_1^\dagger \tilde{d}_1 \rangle & \langle \tilde{d}_1^\dagger \tilde{d}_2 \rangle \\ \langle \tilde{d}_2^\dagger \tilde{d}_1 \rangle & \langle \tilde{d}_2^\dagger \tilde{d}_2 \rangle \end{bmatrix}, \quad (46)$$

these are related through

$$O_d = R_d^\dagger R_h^\dagger \tilde{O}_d R_h R_d. \quad (47)$$

Here  $R_h R_d$  is the overall rotation matrix pertaining to the dot degrees of freedom, see Eq. (35).

At low temperatures, the mapping onto an isotropic Kondo model implies

$$\tilde{O}_d = \begin{bmatrix} \langle \tilde{n}_\uparrow \rangle & 0 \\ 0 & \langle \tilde{n}_\downarrow \rangle \end{bmatrix}, \quad (48)$$

where

$$\langle \tilde{n}_\sigma \rangle = n_{\text{tot}}/2 + \sigma \tilde{M}. \quad (49)$$

Here we have formally separated the occupancies  $\langle \tilde{n}_\sigma \rangle$  into the sum of a spin component and a charge component. The spin component involves the magnetization  $\tilde{M}$  along the direction of the total effective field  $\vec{h}_{\text{tot}}$ . The latter is well described by the universal magnetization curve  $M_K(h_{\text{tot}}/T_K)$  of the Kondo model [see Eq. (B1)]. As for the total dot occupancy  $n_{\text{tot}}$ , deep in the local-moment regime charge fluctuations are mostly quenched at low temperatures, resulting in the near integer valance  $n_{\text{tot}} \approx 1$ . One can slightly improve on this estimate of

$n_{\text{tot}}$  by resorting to first-order perturbation theory in  $\Gamma_\sigma$  (and zeroth order in  $h$ ):

$$n_{\text{tot}} \approx 1 + \frac{\Gamma_\uparrow + \Gamma_\downarrow}{2\pi} \left( \frac{1}{\epsilon_0} + \frac{1}{U + \epsilon_0} \right) = 1 - 2\rho v_+. \quad (50)$$

This low-order process does not enter the Kondo effect, and is not contained in  $M_K(h_{\text{tot}}/T_K)$ .<sup>35</sup> With the above approximations, the combination of Eqs. (47) and (48) yields a general formula for the reduced density matrix

$$O_d = n_{\text{tot}}/2 + M_K(h_{\text{tot}}/T_K) R_d^\dagger R_h^\dagger \tau_z R_h R_d. \quad (51)$$

#### 1. Zero Aharonov-Bohm fluxes

As in the case of the conductance, Eq. (51) considerably simplifies in the absence of Aharonov-Bohm fluxes, when the combined rotation  $R_h R_d$  equals  $(s_R s_\theta)^{1/2} e^{i\tau_y(\theta_h + s_\theta \theta_d)/2} e^{i\pi\tau_z(1-s_\theta)/4}$  [see Eqs. (36) and (A29)]. Explicitly, Eq. (51) becomes

$$O_d = n_{\text{tot}}/2 + M_K(h_{\text{tot}}/T_K) \cos(\theta_d + s_\theta \theta_h) \tau_z + M_K(h_{\text{tot}}/T_K) \sin(\theta_d + s_\theta \theta_h) \tau_x, \quad (52)$$

where the sign  $s_\theta$  and angle  $\theta_d$  are given by Eqs. (A30) and (A23), respectively.

Several observations are apparent from Eq. (52). Firstly, when written in the original “spin” basis  $d_1^\dagger$  and  $d_2^\dagger$ , the reduced density matrix  $O_d$  contains the off-diagonal matrix element  $M_K(h_{\text{tot}}/T_K) \sin(\theta_d + s_\theta \theta_h)$ . The latter reflects the fact that the original “spin” states are inclined with respect to the anisotropy axis dynamically selected by the system. Secondly, similar to the conductance of Eq. (40),  $O_d$  depends on two variables alone:  $\theta_d + s_\theta \theta_h$  and the reduced field  $h_{\text{tot}}/T_K$ . Here, again, the angle  $\theta_d$  depends solely on the tunnelling matrix  $\hat{A}$ , while the sign  $s_\theta$  depends additionally on  $\Delta$  and  $b$ . Thirdly, the original levels  $d_1^\dagger$  and  $d_2^\dagger$  have the occupation numbers

$$\langle n_1 \rangle = n_{\text{tot}}/2 + M_K(h_{\text{tot}}/T_K) \cos(\theta_d + s_\theta \theta_h), \quad (53a)$$

$$\langle n_2 \rangle = n_{\text{tot}}/2 - M_K(h_{\text{tot}}/T_K) \cos(\theta_d + s_\theta \theta_h). \quad (53b)$$

In particular, equal populations  $\langle n_1 \rangle = \langle n_2 \rangle$  are found if either  $h_{\text{tot}}$  is zero or if  $\theta_d + s_\theta \theta_h$  equals  $\pi/2$  up to an integer multiple of  $\pi$ . This provides one with a clear criterion for the occurrence of population inversion,<sup>9,10,13</sup> i.e., the crossover from  $\langle n_1 \rangle > \langle n_2 \rangle$  to  $\langle n_2 \rangle > \langle n_1 \rangle$  or vice versa.

#### 2. Parallel-field configuration

In the parallel-field configuration, the angle  $\theta_h$  is either zero or  $\pi$ , depending on whether the magnetic field  $\vec{h}_{\text{tot}}$  is parallel or antiparallel to the  $z$  axis (recall that  $h \sin \theta =$

$h_{\text{tot}} \sin \theta_h = 0$  in this case). The occupancies  $\langle n_1 \rangle$  and  $\langle n_2 \rangle$  acquire the exact representation

$$\langle n_1 \rangle = n_{\text{tot}}/2 + M \cos \theta_d, \quad (54a)$$

$$\langle n_2 \rangle = n_{\text{tot}}/2 - M \cos \theta_d, \quad (54b)$$

where  $n_{\text{tot}}$  is the exact total occupancy of the dot and  $M = \langle n_\uparrow - n_\downarrow \rangle / 2$  is the dot “magnetization,” defined and used previously (not to be confused with  $\tilde{M} = \pm M$ ). As with the conductance, Eqs. (54) encompass all regimes of the dot, and extend to arbitrary Aharonov-Bohm fluxes. They properly reduce to Eqs. (53) in the Kondo regime, when  $n_{\text{tot}} \approx 1$  [see Eq. (50)] and  $M \rightarrow \pm M_K (h_{\text{tot}}/T_K)$ . [Note that Eqs. (53) have been derived for zero Aharonov-Bohm fluxes.]

One particularly revealing observation that follows from Eqs. (54) concerns the connection between the phenomena of population inversion and phase lapses in the parallel-field configuration. For a given fixed tunnelling matrix  $\hat{A}$  in the parallel-field configuration, the condition for a population inversion to occur is identical to the condition for a phase lapse to occur. Both require that  $M = 0$ . Thus, these seemingly unrelated phenomena are synonymous in the parallel-field configuration. This is not generically the case when  $h_{\text{tot}}^x \neq 0$ , as can be seen, for example, from Eqs. (40) and (53). In the absence of Aharonov-Bohm fluxes, the conductance is proportional to  $\sin^2(\theta_l + s_R \theta_h)$ . It therefore vanishes for  $h_{\text{tot}}^x \neq 0$  only if  $\theta_l + s_R \theta_h = 0 \bmod \pi$ . By contrast, the difference in populations  $\langle n_1 - n_2 \rangle$  involves the unrelated factor  $\cos(\theta_d + s_\theta \theta_h)$ , which generally does not vanish together with  $\sin(\theta_l + s_R \theta_h)$ .

Another useful result which applies to the parallel-field configuration is an exact expression for the  $T = 0$  conductance in terms of the population difference  $\langle n_1 - n_2 \rangle$ . It follows from Eqs. (54) that  $M = \langle n_1 - n_2 \rangle / (2 \cos \theta_d)$ . Inserting this relation into Eq. (44) yields

$$G = \frac{e^2}{2\pi\hbar} \sin^2 \left( \frac{\pi \langle n_1 - n_2 \rangle}{\cos \theta_d} \right) \sin^2 \theta_l. \quad (55)$$

This expression will be used in Sec. V for analyzing the conductance in the presence of isotropic couplings, and for the cases considered by Meden and Marquardt.<sup>11</sup>

## V. RESULTS

Up until this point we have developed a general framework for describing the local-moment regime in terms of two competing energy scales, the Kondo temperature  $T_K$  and the renormalized magnetic field  $h_{\text{tot}}$ . We now turn to explicit calculations that exemplify these ideas. To this end, we begin in Sec. V A with the exactly solvable case  $V_\uparrow = V_\downarrow$ , which corresponds to the conventional Anderson model in a finite magnetic field.<sup>6</sup> Using the exact Bethe *ansatz* solution of the Anderson model,<sup>20</sup> we present a detailed analysis of this special case with three

objectives in mind: (i) to benchmark our general treatment against rigorous results; (ii) to follow in great detail the delicate interplay between the two competing energy scales that govern the low-energy physics; (iii) to set the stage for the complete explanation of the charge oscillations<sup>9,10,13</sup> and the correlation-induced resonances in the conductance of this device.<sup>11,12</sup>

We then proceed in Sec. V B to the generic anisotropic case  $V_\uparrow \neq V_\downarrow$ . Here a coherent explanation is provided for the ubiquitous phase lapses,<sup>8</sup> population inversion,<sup>9,10</sup> and correlation-induced resonances<sup>11,12</sup> that were reported recently in various studies of two-level quantum dots. In particular, we expose the latter resonances as a disguised Kondo phenomenon. The general formulae of Sec. IV are quantitatively compared to the numerical results of Ref.11. The detailed agreement that is obtained nicely illustrates the power of the analytical approach put forward in this paper.

### A. Exact treatment of $V_\uparrow = V_\downarrow$

As emphasized in Sec. III, all tunnelling matrices  $\hat{A}$  which satisfy Eq. (11) give rise to equal amplitudes  $V_\uparrow = V_\downarrow = V$  within the Anderson Hamiltonian description of Eq. (7). Given this extra symmetry, one can always choose the unitary matrices  $R_l$  and  $R_d$  in such a way that the magnetic field  $h$  points along the  $z$  direction [namely,  $\cos \theta = 1$  in Eq. (7)]. Perhaps the simplest member in this class of tunnelling matrices is the case where  $a_{L1} = -a_{L2} = a_{R1} = a_{R2} = V/\sqrt{2}$ ,  $\varphi_L = \varphi_R = 0$  and  $b = 0$ . One can simply convert the conduction-electron operators to even and odd combinations of the two leads, corresponding to choosing  $\theta_l = \pi/2 + \theta_d$ . Depending on the sign of  $\Delta$ , the angle  $\theta_d$  is either zero (for  $\Delta < 0$ ) or  $\pi$  (for  $\Delta > 0$ ), which leaves us with a conventional Anderson impurity in the presence of the magnetic field  $\vec{h} = |\Delta| \hat{z}$ . All other rotation angle that appear in Eqs. (A2) and (A2) (i.e.,  $\chi$ 's and  $\phi$ 's) are equal to zero. For concreteness we shall focus hereafter on this particular case, which represents, up to a simple rotation of the  $d_\sigma^\dagger$  and  $c_{k\sigma}^\dagger$  operators, all tunnelling matrices  $\hat{A}$  in this category of interest. Our discussion is restricted to zero temperature.

#### 1. Impurity magnetization

We have solved the exact Bethe *ansatz* equations numerically using the procedure outlined in Appendix B. Our results for the occupation numbers  $\langle n_\sigma \rangle$  and the magnetization  $M = \langle n_\uparrow - n_\downarrow \rangle / 2$  are summarized in Figs. 2 and 3. Figure 2 shows the magnetization of the Anderson impurity as a function of the (average) level position  $\epsilon_0$  in a constant magnetic field,  $h = \Delta = 10^{-3}U$ . The complementary regime  $\epsilon_0 < -U/2$  is obtained by a simple reflection about  $\epsilon_0 = -U/2$ , as follows from

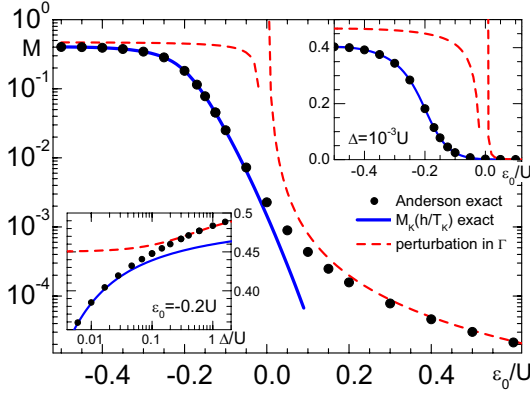


FIG. 2: (Color online) Magnetization of the isotropic case as a function of  $\epsilon_0$ : exact Bethe *ansatz* curve and comparison with different approximation schemes. Black symbols show the magnetization  $M$  derived from the exact Bethe *ansatz* equations; the dashed (red) line marks the result of first-order perturbation theory in  $\Gamma$  (Ref.9, divergent at  $\epsilon_0 = 0$ ); the thick (blue) line is the analytical formula for the magnetization in the Kondo limit, Eq. (B1), with  $T_K$  given by Eq. (B4). The model parameters are  $\Gamma/U = 0.05$ ,  $\Delta/U = 10^{-3}$  and  $T = 0$ . The upper right inset shows the same data but on a linear scale. The lower left inset shows the magnetization  $M$  as a function of the magnetic field  $h = \Delta$  at fixed  $\epsilon_0/U = -0.2$ . The universal magnetization curve of the Kondo model well describes the exact magnetization up to  $M \approx 0.42$  (lower fields not shown), while first-order perturbation theory in  $\Gamma$  fails from  $M \approx 0.46$  downwards.

the particle-hole transformation  $d_\sigma \rightarrow d_{-\sigma}^\dagger$  and  $c_{k\sigma} \rightarrow -c_{k-\sigma}^\dagger$ . The Bethe *ansatz* curve accurately crosses over from the perturbative domain at large  $\epsilon_0 \gg \Gamma$  (when the dot is almost empty) to the local-moment regime with a fully pronounced Kondo effect (when the dot is singly occupied). In the latter regime, we find excellent agreement with the analytical magnetization curve of the Kondo model, Eq. (B1), both as a function of  $\epsilon_0$  and as a function of the magnetic field  $\Delta$  (lower left inset to Fig. 2). The agreement with the universal Kondo curve is in fact quite surprising in that it extends nearly into the mixed-valent regime. As a function of field, the Kondo curve of Eq. (B1) applies up to fields of the order of  $h \sim \sqrt{\Gamma U} \gg T_K$ .

## 2. Occupation numbers and charge oscillations

Figure 3 displays the individual occupation numbers  $\langle n_1 \rangle$  and  $\langle n_2 \rangle$  as a function of  $\epsilon_0$ , for a series of constant fields  $h = \Delta$ . In going from large  $\epsilon_0 \gg \Gamma$  to large  $-(\epsilon_0 + U) \gg \Gamma$ , the total charge of the quantum dot increases monotonically from nearly zero to nearly two. However, the partial occupancies  $\langle n_1 \rangle$  and  $\langle n_2 \rangle$  display nonmonotonicities, which have drawn considerable theoretical attention lately.<sup>9,10,13</sup> As seen in Fig. 3, the nonmonotonicities can be quite large, although no popula-

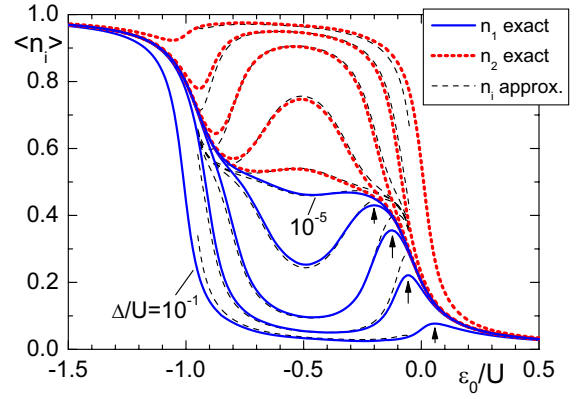


FIG. 3: (Color online) The occupation numbers  $\langle n_1 \rangle$  [solid (blue) lines] and  $\langle n_2 \rangle$  [dotted (red) lines] versus  $\epsilon_0$ , as obtained from the solution of the exact Bethe *ansatz* equations. In going from the inner-most to the outer-most pairs of curves, the magnetic field  $h = \Delta$  increases by a factor of 10 between each successive pair of curves, with the inner-most (outer-most) curves corresponding to  $\Delta/U = 10^{-5}$  ( $\Delta/U = 0.1$ ). The remaining model parameters are  $\Gamma/U = 0.05$  and  $T = 0$ . Nonmonotonicities are seen in the process of charging. These are most pronounced for intermediate values of the field. The evolution of the nonmonotonicities with increasing field is tracked by arrows. The dashed black lines show the approximate values calculated from Eqs. (53) and (50) based on the mapping onto the Kondo Hamiltonian (here  $\theta_h = 0$  and  $\theta_d = \pi$ ).

tion inversion occurs for  $\Gamma_\uparrow = \Gamma_\downarrow$ .

Our general discussion in Sec. III makes it is easy to interpret these features of the partial occupancies  $\langle n_i \rangle$ . Indeed, as illustrated in Fig. 3, there is excellent agreement in the local-moment regime between the exact Bethe *ansatz* results and the curves obtained from Eqs. (53) and (50) based on the mapping onto the Kondo Hamiltonian. We therefore utilize Eqs. (53) for analyzing the data. To begin with we note that, for  $\Gamma_\uparrow = \Gamma_\downarrow$ , there is no renormalization of the effective magnetic field. The latter remains constant and equal to  $h = \Delta$  independent of  $\epsilon_0$ . Combined with the fact that  $\cos(\theta_d + s_\theta \theta_h) \equiv -1$  in Eqs. (53), the magnetization  $M = (\langle n_\uparrow - n_\downarrow \rangle)/2 = (\langle n_2 - n_1 \rangle)/2$  depends exclusively on the ratio  $\Delta/T_K$ . The sole dependence on  $\epsilon_0$  enters through  $T_K$ , which varies according to Eq. (B4). Thus,  $M$  is positive for all gate voltages  $\epsilon_0$ , excluding the possibility of a population inversion.

The nonmonotonicities in the individual occupancies stem from the explicit dependence of  $T_K$  on the gate voltage  $\epsilon_0$ . According to Eq. (B4),  $T_K$  is minimal in the middle of the Coulomb-blockade valley, increasing monotonically as a function of  $|\epsilon_0 + U/2|$ . Thus,  $\Delta/T_K$ , and consequently  $M$ , is maximal for  $\epsilon_0 = -U/2$ , decreasing monotonically the farther  $\epsilon_0$  departs from  $-U/2$ . Since  $n_{\text{tot}} \approx 1$  is nearly a constant in the local-moment regime, this implies the following evolution of the partial occupancies:  $\langle n_1 \rangle$  decreases ( $\langle n_2 \rangle$  increases) as  $\epsilon_0$  is lowered from roughly zero to  $-U/2$ . It then increases (decreases)

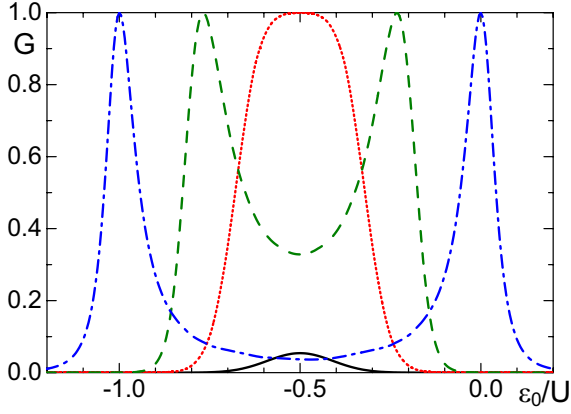


FIG. 4: (Color online) The exact conductance  $G$  [in units of  $e^2/(2\pi\hbar)$ ] versus  $\epsilon_0$ , as obtained from the Bethe *ansatz* magnetization  $M$  and Eq. (55) with  $\theta_l = 3\pi/2$  and  $\theta_d = \pi$ . Here  $\Delta/U$  equals  $10^{-5}$  [full (black) line],  $10^{-4}$  [dotted (red) line],  $10^{-3}$  [dashed (green) line] and  $0.1$  [dot-dashed (blue) line]. The remaining model parameters are  $\Gamma/U = 0.05$  and  $T = 0$ . Once  $\Delta$  exceeds the critical field  $h_c \approx 2.4T_K^{\min}$ , the single peak at  $\epsilon_0 = -U/2$  is split into two correlation-induced peaks, which cross over to Coulomb-blockade peaks at large  $\Delta$ .

as  $\epsilon_0$  is further lowered toward  $-U$ . Combined with the crossovers to the empty-impurity and doubly occupied regimes, this generates a local maximum (minimum) in  $\langle n_1 \rangle$  ( $\langle n_2 \rangle$ ) near  $\epsilon_0 \sim 0$  ( $\epsilon_0 \sim -U$ ).

Note that the local extremum in  $\langle n_i \rangle$  is most pronounced for intermediate values of the field  $\Delta$ . This can be understood by examining the two most relevant energy scales in the problem, namely, the minimal Kondo temperature  $T_K^{\min} = T_K|_{\epsilon_0 = -U/2}$  and the hybridization width  $\Gamma$ . These two energies govern the spin susceptibility of the impurity in the middle of the Coulomb-blockade valley (when  $\epsilon_0 = -U/2$ ) and in the mixed-valent regime (when either  $\epsilon_0 \approx 0$  or  $\epsilon \approx -U$ ), respectively. The charging curves of Fig. 3 stem from an interplay of the three energy scales  $\Delta$ ,  $T_K^{\min}$  and  $\Gamma$  as described below.

When  $\Delta \ll T_K^{\min}$ , exemplified by the pair of curves corresponding to the smallest field  $\Delta = 10^{-5}U \approx 0.24T_K^{\min}$  in Fig. 3, the magnetic field remains small throughout the Coulomb-blockade valley and no significant magnetization develops. The two levels are roughly equally populated, showing a plateau at  $\langle n_1 \rangle \approx \langle n_2 \rangle \approx 1/2$  in the regime where the dot is singly occupied. As  $\Delta$  grows and approaches  $T_K^{\min}$ , the field becomes sufficiently strong to significantly polarize the impurity in the vicinity of  $\epsilon_0 = -U/2$ . A gap then rapidly develops between  $\langle n_1 \rangle$  and  $\langle n_2 \rangle$  near  $\epsilon_0 = -U/2$  as  $\Delta$  is increased. Once  $\Delta$  reaches the regime  $T_K^{\min} \ll \Delta \ll \Gamma$ , a crossover from  $h \gg T_K$  (fully polarized impurity) to  $h \ll T_K$  (unpolarized impurity) occurs as  $\epsilon_0$  is tuned away from the middle of the Coulomb-blockade valley. This leads to the development of a pronounced maximum (minimum) in  $\langle n_1 \rangle$  ( $\langle n_2 \rangle$ ), as marked by the arrows in Fig. 3. Finally, when  $h \gtrsim \Gamma$ , the field is sufficiently large to keep

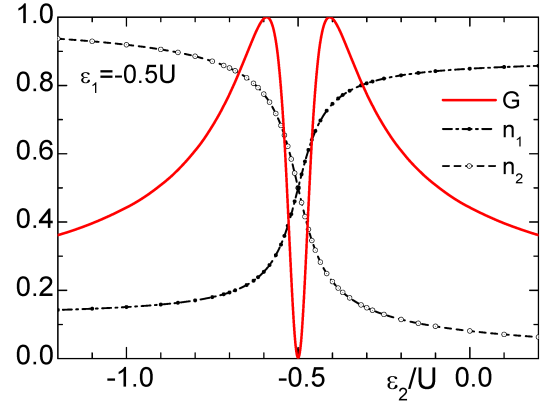


FIG. 5: (Color online) The exact occupation numbers  $\langle n_i \rangle$  and conductance  $G$  [in units of  $e^2/(2\pi\hbar)$ ] as a function of  $\epsilon_2$ , for  $T = 0$ ,  $\Gamma/U = 0.2$  and fixed  $\epsilon_1/U = -1/2$ . The population inversion at  $\epsilon_2 = \epsilon_1$  leads to a sharp transmission zero (phase lapse). Note the general resemblance between the functional dependence of  $G$  on  $\epsilon_2$  and the correlation-induced resonances reported by Meden and Marquardt<sup>11</sup> for  $\Gamma_\uparrow \neq \Gamma_\downarrow$  (see Fig. 6).

the dot polarized throughout the local-moment regime. The extremum in  $\langle n_i \rangle$  degenerates into a small bump in the vicinity of either  $\epsilon_0 \approx 0$  or  $\epsilon_0 \approx -U$ , which is the non-monotonic feature first discussed in Ref.9. This regime is exemplified by the pair of curves corresponding to the largest field  $\Delta = 0.1U = 2\Gamma$  in Fig. 3, whose parameters match those used in Fig. 2 of Ref.9. Note, however, that the perturbative calculations of Ref.9 will inevitably miss the regime  $T_K^{\min} \ll \Delta \ll \Gamma$  where this feature is large.<sup>36</sup>

### 3. Conductance

The data of Fig. 3 can easily be converted to conductance curves by using the exact formula of Eq. (55) with  $\theta_l = 3\pi/2$  and  $\theta_d = \pi$ . The outcome is presented in Fig. 4. The evolution of  $G(\epsilon_0)$  with increasing  $\Delta$  is quite dramatic. When  $\Delta$  is small, the conductance is likewise small with a shallow peak at  $\epsilon_0 = -U/2$ . This peak steadily grows with increasing  $\Delta$  until reaching the unitary limit, at which point it is split in two. Upon further increasing  $\Delta$ , the two split peaks gradually depart, approaching the peak positions  $\epsilon_0 \approx 0$  and  $\epsilon_0 \approx -U$  for large  $\Delta$ . The conductance at each of the two maxima remains pinned at all stages at the unitary limit.

These features of the conductance can be naturally understood based on Eqs. (55) and (53). When  $\Delta \ll T_K^{\min}$ , the magnetization  $M \approx \Delta/(2\pi T_K)$  and the conductance  $G \approx (\Delta/T_K)^2 e^2/(2\pi\hbar)$  are uniformly small, with a peak at  $\epsilon_0 = -U/2$  where  $T_K$  is the smallest. The conductance monotonically grows with increasing  $\Delta$  until reaching the critical field  $\Delta = h_c \approx 2.4T_K^{\min}$ , where  $M|_{\epsilon_0 = -U/2} = 1/4$  and  $G|_{\epsilon_0 = -U/2} = e^2/(2\pi\hbar)$ . Upon further increasing  $\Delta$ , the magnetization at  $\epsilon_0 = -U/2$  exceeds  $1/4$ , and the associated conductance decreases. The unitarity condition

$M = 1/4$  is satisfied at two gate voltages  $\epsilon_{\pm}^{\max}$  symmetric about  $-U/2$ , defined by the relation  $T_K \approx \Delta/2.4$ . From Eq. (B4) one obtains

$$\epsilon_{\pm}^{\max} = -\frac{U}{2} \pm \sqrt{\frac{U^2}{4} - \Gamma^2 + \frac{2\Gamma U}{\pi} \ln\left(\frac{\pi\Delta}{2.4\sqrt{2\Gamma U}}\right)}. \quad (56)$$

The width of the two conductance peaks,  $\Delta\epsilon$ , can be estimated for  $T_K^{\min} \ll \Delta \ll \Gamma$  from the inverse of the derivative  $d(\Delta/T_K)/d\epsilon_0$ , evaluated at  $\epsilon_0 = \epsilon_{\pm}^{\max}$ . It yields

$$\Delta\epsilon \sim \frac{\Gamma U}{\pi|\epsilon_{\pm}^{\max} + U/2|}. \quad (57)$$

Finally, when  $\Delta > \Gamma$ , the magnetization exceeds  $1/4$  throughout the local-moment regime. The resonance condition  $M = 1/4$  is met only as charge fluctuations become strong, namely, for either  $\epsilon_0 \approx 0$  or  $\epsilon_0 \approx -U$ . The resonance width  $\Delta\epsilon$  evolves continuously in this limit to the standard result for the Coulomb-blockade resonances,  $\Delta\epsilon \sim \Gamma$ .

Up until now the energy difference  $\Delta$  was kept constant while tuning the average level position  $\epsilon_0$ . This protocol, which precludes population inversion as a function of the control parameter, best suits a single-dot realization of our model, where both levels can be uniformly tuned using a single gate voltage. In the alternative realization of two spatially separated quantum dots, each controlled by its own separate gate voltage, one could fix the energy level  $\epsilon_1 = \epsilon_0 + \Delta/2$  and sweep the other level,  $\epsilon_2 = \epsilon_0 - \Delta/2$ . This setup amounts to changing the field  $h$  externally, and is thus well suited for probing the magnetic response of our effective impurity.

An example for such a protocol is presented in Fig. 5, where  $\epsilon_1$  is held fixed at  $\epsilon_1 = -U/2$ . As  $\epsilon_2$  is swept through  $\epsilon_1$ , a population inversion takes place, leading to a narrow dip in the conductance. The width of the conductance dip is exponentially small due to Kondo correlations. Indeed, one can estimate the dip width,  $\Delta\epsilon_{\text{dip}}$ , from the condition  $|\epsilon_1 - \epsilon_2| = T_K|_{\epsilon_2=\epsilon_1}$ , which yields

$$\Delta\epsilon_{\text{dip}} \sim \sqrt{U\Gamma} \exp\left(-\frac{\pi U}{8\Gamma}\right). \quad (58)$$

### B. Anisotropic couplings, $\Gamma_{\uparrow} \neq \Gamma_{\downarrow}$

As demonstrated at length in Sec. V A, the occurrence of population inversion and a transmission zero for  $\Gamma_{\uparrow} = \Gamma_{\downarrow}$  requires an external modulation of the effective magnetic field. Any practical device will inevitably involve, though, some tunnelling anisotropy,  $V_{\uparrow} \neq V_{\downarrow}$ . The latter provides a different route for changing the effective magnetic field, through the anisotropy-induced terms in Eq. (30). Implementing the same protocol as in Sec. V A 2 (that is, uniformly sweeping the average level position  $\epsilon_0$  while keeping the difference  $\Delta$  constant) would now generically result both in population inversion

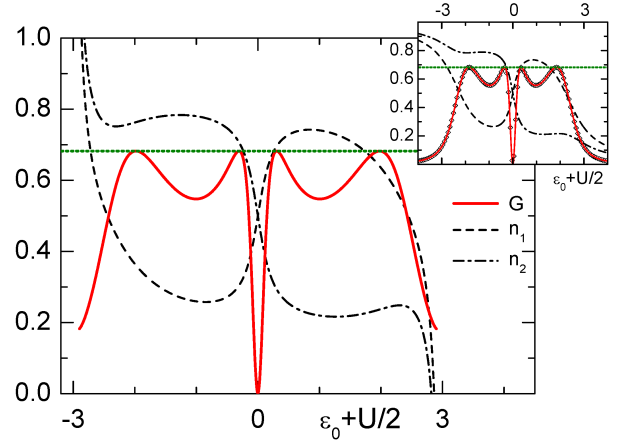


FIG. 6: The occupation numbers  $\langle n_i \rangle$  and conductance  $G$  [in units of  $e^2/(2\pi\hbar)$ ] as a function of  $\epsilon_0 + U/2$  [in units of  $\Gamma_{\text{tot}} = (\Gamma_{\uparrow} + \Gamma_{\downarrow})$ ], calculated from Eqs. (40) and (53) based on the mapping onto the Kondo model. The model parameters are identical to those used in Fig. 2 of Ref.11, lower left panel:  $h = \varphi = 0$ ,  $U/\Gamma_{\text{tot}} = 6$ ,  $\Gamma_{\uparrow}/\Gamma_{\text{tot}} = 0.62415$  and  $T = 0$ . The explicit tunnelling matrix elements are detailed in Eq. (59), corresponding to the rotation angles  $\theta_l = 2.1698$  and  $\theta_d = -0.63434$  (measured in radians). The angle  $\theta_h$  equals zero. The inset shows functional renormalization-group (FRG) data as defined in Ref.11, corrected for the renormalization of the two-particle vertex.<sup>12,37</sup> The small symbols in the inset show the conductance as calculated from the FRG occupation numbers using our Eq. (55). The horizontal dotted lines in each plot mark the maximal conductance predicted by Eq. (55),  $(e^2/2\pi\hbar) \sin^2 \theta_l$ .

and a transmission zero due to the rapid change in direction of the total field  $\vec{h}_{\text{tot}}$ . As emphasized in Sec. IV B 2, the two phenomena will generally occur at different gate voltages when  $V_{\uparrow} \neq V_{\downarrow}$ .

#### 1. Degenerate levels, $\Delta = b = 0$

We begin our discussion with the case where  $\Delta = b = 0$ , which was extensively studied in Ref.11. It corresponds to a particular limit of the parallel-field configuration where  $h = 0$ . In the parallel-field configuration, the conductance  $G$  and occupancies  $\langle n_i \rangle$  take the exact forms specified in Eqs. (44) and (54), respectively. These expressions reduce in the Kondo regime to Eqs. (40) and (53), with  $\theta_h$  either equal to zero or  $\pi$ , depending on the sign of  $h_{\text{tot}}^z$ .

Figure 6 shows the occupation numbers and the conductance obtained from Eqs. (40) and (53), for  $\Delta = b = 0$  and the particular tunnelling matrix used in Fig. 2 of Ref.11:

$$\hat{A} = A_0 \begin{bmatrix} \sqrt{0.27} & \sqrt{0.16} \\ \sqrt{0.33} & -\sqrt{0.24} \end{bmatrix}. \quad (59)$$

Here  $A_0$  equals  $\sqrt{\Gamma_{\text{tot}}/(\pi\rho)}$ , with  $\Gamma_{\text{tot}} = \Gamma_{\uparrow} + \Gamma_{\downarrow}$  being the combined hybridization width. The Coulomb repulsion  $U$

is set equal to  $6\Gamma_{\text{tot}}$ , matching the value used in the lower left panel of Fig. 2 in Ref.11. For comparison, the corresponding functional renormalization-group (fRG) data of Ref.11 is shown in the inset, after correcting for the renormalization of the two-particle vertex.<sup>12,37</sup> The accuracy of the fRG has been established<sup>11,12</sup> up to moderate values of  $U/\Gamma_{\text{tot}} \sim 10$  through a comparison with Wilson's numerical renormalization-group method.<sup>38</sup> Including the renormalization of the two-particle vertex further improves the fRG data as compared to that of Ref.11, as reflected, e.g., in the improved position of the outer pair of conductance resonances.

The agreement between our analytical approach and the fRG is evidently very good in the local-moment regime, despite the rather moderate value of  $U/\Gamma_{\text{tot}}$  used. Noticeable deviations develop in  $\langle n_i \rangle$  only as the mixed-valent regime is approached (for  $\epsilon_0 \gtrsim -\Gamma_{\text{tot}}$  or  $\epsilon + U \lesssim \Gamma_{\text{tot}}$ ), where our approximations naturally break down. In particular, our approach accurately describes the phase lapse at  $\epsilon_0 = -U/2$ , the inversion of population at the same gate voltage, the location and height of the correlation-induced resonances, and even the location and height of the outer pair of conductance resonances. Most importantly, our approach provides a coherent analytical picture for the physics underlying these various features, as elaborated below.

Before proceeding to elucidate the underlying physics, we briefly quote the relevant parameters that appear in the conversion to the generalized Anderson model of Eq. (7). Using the prescriptions detailed in Appendix A, the hybridization widths  $\Gamma_\sigma = \pi\rho V_\sigma^2$  come out to be

$$\Gamma_\uparrow/\Gamma_{\text{tot}} = 0.62415, \quad \Gamma_\downarrow/\Gamma_{\text{tot}} = 0.36585, \quad (60)$$

while the angles of rotation equal

$$\theta_l = 2.1698, \quad \theta_d = -0.63434. \quad (61)$$

Here  $\theta_l$  and  $\theta_d$  are quoted in radians. Using the exact conductance formula of Eq. (44),  $G$  is predicted to be bounded by the maximal conductance

$$G_{\text{max}} = \frac{e^2}{2\pi\hbar} \sin^2 \theta_l = 0.68210 \frac{e^2}{2\pi\hbar}, \quad (62)$$

obtained whenever the magnetization  $M = \langle n_\uparrow - n_\downarrow \rangle/2$  is equal to  $\pm 1/4$ . The heights of the fRG resonances are in excellent agreement with Eq. (62). Indeed, as demonstrated in the inset to Fig. 6, the fRG occupancies and conductance comply to within extreme precision with the exact relation of Eq. (55). As for the functional form of the Kondo temperature  $T_K$ , its exponential dependence on  $\epsilon_0$  is very accurately described by Eq. (29). In the absence of a precise expression for the pre-exponential factor when  $\Gamma_\uparrow \neq \Gamma_\downarrow$ , we employ the expression

$$T_K = (\sqrt{U\Gamma_{\text{tot}}}/\pi) \exp \left[ \frac{\pi\epsilon_0(U + \epsilon_0)}{2U(\Gamma_\uparrow - \Gamma_\downarrow)} \ln \frac{\Gamma_\uparrow}{\Gamma_\downarrow} \right], \quad (63)$$

which properly reduces to Eq. (B4) (up to the small  $\Gamma^2$  correction in the exponent) when  $\Gamma_\uparrow = \Gamma_\downarrow = \Gamma$ .

The occupancies and conductance of Fig. 6 can be fully understood from our general discussion in Sec. III. Both quantities follow from the magnetization  $M$ , which vanishes at  $\epsilon_0 = -U/2$  due to particle-hole symmetry. As a consequence, the two levels are equally populated at  $\epsilon_0 = -U/2$  and the conductance vanishes [see Eqs. (44) and (54)]. Thus, there is a simultaneous phase lapse and an inversion of population at  $\epsilon_0 = -U/2$ , which is a feature generic to  $\Delta = b = 0$  and arbitrary  $\hat{A}$ . As soon as the gate voltage is removed from  $-U/2$ , i.e.,  $\epsilon_0 = -U/2 + \delta\epsilon$  with  $\delta\epsilon \neq 0$ , a finite magnetization develops due to the appearance of a finite effective magnetic field  $\vec{h}_{\text{tot}} = h_{\text{tot}}^z \hat{z}$  with

$$h_{\text{tot}}^z \approx \frac{\Gamma_\uparrow - \Gamma_\downarrow}{\pi} \ln \frac{1 + 2\delta\epsilon/U}{1 - 2\delta\epsilon/U} \quad (64)$$

[see Eq. (33)]. Note that the sign of  $h_{\text{tot}}^z$  coincides with that of  $\delta\epsilon$ , hence  $M$  is positive (negative) for  $\epsilon_0 > -U/2$  ( $\epsilon_0 < -U/2$ ). Since  $\cos \theta_d > 0$  for the model parameters used in Fig. 6, it follows from Eq. (54) that  $\langle n_1 \rangle > \langle n_2 \rangle$  ( $\langle n_1 \rangle < \langle n_2 \rangle$ ) for  $\epsilon_0 > -U/2$  ( $\epsilon_0 < -U/2$ ), as is indeed found in Fig. 6. Once again, this result is generic to  $\Delta = b = 0$ , except for the sign of  $\cos \theta_d$  which depends on details of the tunnelling matrix  $\hat{A}$ .

In contrast with the individual occupancies, the conductance  $G$  depends solely on the magnitude of  $M$ , and is therefore a symmetric function of  $\delta\epsilon$ . Similar to the rich structure found for  $\Gamma_\uparrow = \Gamma_\downarrow$  and  $\Delta > 0$  in Fig. 4, the intricate conductance curve in Fig. 6 is the result of the interplay between  $h_{\text{tot}}^z$  and  $T_K$ , and the nonmonotonic dependence of  $G$  on  $|M|$ . The basic physical picture is identical to that in Fig. 4, except for the fact that the effective magnetic field  $h_{\text{tot}}^z$  is now itself a function of the gate voltage  $\epsilon_0$ .

As a rule, the magnetization  $|M|$  first increases with  $|\delta\epsilon|$  due to the rapid increase in  $h_{\text{tot}}^z$ . It reaches its maximal value  $M_{\text{max}}$  at some intermediate  $|\delta\epsilon|$  before decreasing again as  $|\delta\epsilon|$  is further increased. Inevitably  $|M|$  becomes small again once  $|\delta\epsilon|$  exceeds  $U/2$ . The shape of the associated conductance curve depends crucially on the magnitude of  $M_{\text{max}}$ , which monotonically increases as a function of  $U$ . When  $M_{\text{max}} < 1/4$ , the conductance features two symmetric maxima, one on each side of the particle-hole symmetric point. Each of these peaks is analogous to the one found in Fig. 4 for  $\Delta < h_c$ . Their height steadily grows with increasing  $U$  until the unitarity condition  $M_{\text{max}} = 1/4$  is met. This latter condition defines the critical repulsion  $U_c$  found in Ref.11. For  $U > U_c$ , the maximal magnetization  $M_{\text{max}}$  exceeds one quarter. Hence the unitarity condition  $M = \pm 1/4$  is met at two pairs of gate voltages, one pair of gate voltages on either side of the particle-hole symmetric point  $\epsilon_0 = -U/2$ . Each of the single resonances for  $U < U_c$  is therefore split in two, with the inner pair of peaks evolving into the correlation-induced resonances of Ref.11. The point of maximal magnetization now shows up as a local minimum of the conductance, similar to the point  $\epsilon_0 = -U/2$  in Fig. 4 when  $\Delta > h_c$ .



For large  $U \gg \Gamma_{\text{tot}}$ , the magnetization  $|M|$  grows rapidly as one departs from  $\epsilon_0 = -U/2$ , due to the exponential smallness of the Kondo temperature  $T_K|_{\epsilon_0=-U/2}$ . The dot remains polarized throughout the local-moment regime, losing its polarization only as charge fluctuations become strong. In this limit the inner pair of resonances lie exponentially close to  $\epsilon_0 = -U/2$  (see below), while the outer pair of resonances approach  $|\delta\epsilon| \approx U/2$  (the regime of the conventional Coulomb blockade).

The description of this regime can be made quantitative by estimating the position  $\pm\delta\epsilon_{\text{CIR}}$  of the correlation-induced resonances. Since  $M \rightarrow M_K(h_{\text{tot}}^z/T_K)$  deep in the local-moment regime, and since  $\delta\epsilon_{\text{CIR}} \ll \Gamma_{\text{tot}}$  for  $\Gamma_{\text{tot}} \ll U$ , the correlation-induced resonances are peaked at the two gate voltages where  $h_{\text{tot}}^z \approx \pm 2.4T_K|_{\epsilon_0=-U/2}$ . Expanding Eq. (64) to linear order in  $\delta\epsilon_{\text{CIR}}/U \ll 1$  and using Eq. (63) one finds

$$\begin{aligned} \delta\epsilon_{\text{CIR}} &\approx 0.6 \frac{\pi U}{\Gamma_{\uparrow} - \Gamma_{\downarrow}} T_K|_{\epsilon_0=-U/2} \\ &= 0.6 \frac{U\sqrt{U\Gamma_{\text{tot}}}}{\Gamma_{\uparrow} - \Gamma_{\downarrow}} \exp\left[\frac{-\pi U \ln(\Gamma_{\uparrow}/\Gamma_{\downarrow})}{8(\Gamma_{\uparrow} - \Gamma_{\downarrow})}\right]. \end{aligned} \quad (65)$$

Here the pre-exponential factor in the final expression for  $\delta\epsilon_{\text{CIR}}$  is of the same accuracy as that in Eq. (63).

We note in passing that the shape of the correlation-induced resonances and the intervening dip can be conveniently parameterized in terms of the peak position  $\delta\epsilon_{\text{CIR}}$  and the peak conductance  $G_{\text{max}}$ . Expanding Eq. (64) to linear order in  $\delta\epsilon/U \ll 1$  and using Eq. (44) one obtains

$$G(\delta\epsilon) = G_{\text{max}} \sin^2\left[2\pi M_K\left(\frac{2.4\delta\epsilon}{\delta\epsilon_{\text{CIR}}}\right)\right], \quad (66)$$

where  $M_K(h/T_K)$  is the universal magnetization curve of the Kondo model [given explicitly by (B1)]. This parameterization in terms of two easily extractable parameters may prove useful for analyzing future experiments.

It is instructive to compare Eq. (65) for  $\delta\epsilon_{\text{CIR}}$  with the fRG results of Ref.11, which tend to overestimate  $\delta\epsilon_{\text{CIR}}$ . For the special case where  $a_{L1} = a_{R1}$  and  $a_{L2} = -a_{R2}$ , an analytic expression was derived for  $\delta\epsilon_{\text{CIR}}$  based on the fRG.<sup>11</sup> The resulting expression, detailed in Eq. (4) of Ref.11, shows an exponential dependence nearly identical to that of Eq. (65), but with an exponent that is smaller in magnitude by a factor of  $\pi^2/8 \approx 1.23$ .<sup>39</sup> The same numerical factor appears to distinguish the fRG and the numerical renormalization-group data depicted in Fig. 3 of Ref.11, supporting the accuracy of our Eq. (65). It should be emphasized, however, that Fig. 3 of Ref.11 pertains to the tunnelling matrix of Eq. (59) rather than the special case referred to above.

We conclude the discussion of the case where  $\Delta = b = 0$  with accurate results on the renormalized dot levels when the dot is tuned to the peaks of the correlation-induced resonances. The renormalized dot levels,  $\tilde{\epsilon}_{\uparrow}$  and  $\tilde{\epsilon}_{\downarrow}$ , can be defined through the  $T = 0$  retarded dot Green

functions at the Fermi energy:

$$G_{\sigma}(\epsilon = 0) = \frac{1}{-\tilde{\epsilon}_{\sigma} + i\Gamma_{\sigma}}. \quad (67)$$

Here, in writing the Green functions of Eq. (67), we have made use of the fact that the imaginary parts of the retarded dot self-energies,  $-\Gamma_{\sigma}$ , are unaffected by the Coulomb repulsion  $U$  at zero temperature at the Fermi energy. The energies  $\tilde{\epsilon}_{\sigma}$  have the exact representation<sup>21</sup>  $\tilde{\epsilon}_{\sigma} = \Gamma_{\sigma} \cot \delta_{\sigma}$  in terms of the associated phase shifts  $\delta_{\sigma} = \pi \langle n_{\sigma} \rangle$ . Since  $M = \pm 1/4$  at the peaks of the correlation-induced resonances, this implies that  $\delta_{\sigma} = \pi/2 \pm \sigma\pi/4$ , where we have set  $n_{\text{tot}} = 1$ .<sup>40</sup> Thus, the renormalized dot levels take the form  $\tilde{\epsilon}_{\sigma} = \mp \sigma \Gamma_{\sigma}$ , resulting in

$$\tilde{\epsilon}_{\uparrow} \tilde{\epsilon}_{\downarrow} = -\Gamma_{\uparrow} \Gamma_{\downarrow}. \quad (68)$$

The relation specified in Eq. (68) was found in Ref.11, for the special case where  $a_{L1} = a_{R1}$  and  $a_{L2} = -a_{R2}$ .<sup>39</sup> Here it is seen to be a generic feature of the correlation-induced resonances for  $\Delta = b = 0$  and arbitrary  $\hat{A}$ .

## 2. Nondegenerate levels: arbitrary $\Delta$ and $b$

Once  $\sqrt{\Delta^2 + b^2} \neq 0$ , the conductance and the partial occupancies can have a rather elaborate dependence on the gate voltage  $\epsilon_0$ . As implied by the general discussion in Sec. III, the underlying physics remains driven by the competing effects of the polarizing field  $h_{\text{tot}}$  and the Kondo temperature  $T_K$ . However, the detailed dependencies on  $\epsilon_0$  can be quite involving and not as revealing. For this reason we shall not seek a complete characterization of the conductance  $G$  and the partial occupancies  $\langle n_i \rangle$  for arbitrary couplings. Rather, we shall focus on the case where no Aharonov-Bohm fluxes are present and ask two basic questions: (i) under what circumstances is the phenomenon of a phase lapse generic? (ii) under what circumstances is a population inversion generic?

When  $\varphi_L = \varphi_R = 0$ , the conductance and the partial occupancies are given by Eqs. (40) and (53), respectively. Focusing on  $G$  and on  $\langle n_1 - n_2 \rangle$ , these quantities share a common form, with factorized contributions of the magnetization  $M_K$  and the rotation angles. The factors containing  $M_K(h_{\text{tot}}/T_K)$  never vanish when  $h \sin \theta \neq 0$ , since  $h_{\text{tot}}$  always remains positive. This distinguishes the generic case from the parallel-field configuration considered above, where phase lapses and population inversions are synonymous with  $M = 0$ . Instead, the conditions for phase lapses and population inversions to occur become distinct once  $h \sin \theta \neq 0$ , originating from the independent factors where the rotation angles appear. For a phase lapse to develop, the combined angle  $\theta_l + s_R \theta_h$  must equal an integer multiple of  $\pi$ . By contrast, the inversion of population requires that  $\theta_d + s_{\theta} \theta_h = \pi/2 \bmod \pi$ . Here the dependence on the gate voltage  $\epsilon_0$  enters solely through the angle  $\theta_h$ , which specifies the orientation of

the effective magnetic field  $\vec{h}_{\text{tot}}$  [see Eq. (33)]. Since the rotation angles  $\theta_l$  and  $\theta_d$  are generally unrelated, this implies that the two phenomena will typically occur, if at all, at different gate voltages.

For phase lapses and population inversions to be ubiquitous, the angle  $\theta_h$  must change considerably as  $\epsilon_0$  is swept across the Coulomb-blockade valley. In other words, the effective magnetic field  $\vec{h}_{\text{tot}}$  must nearly flip its orientation in going from  $\epsilon_0 \approx 0$  to  $\epsilon_0 \approx -U$ . Since the  $x$  component of the field is held fixed at  $h_{\text{tot}}^x = h \sin \theta > 0$ , this means that its  $z$  component must vary from  $h_{\text{tot}}^z \gg h_{\text{tot}}^x$  to  $-h_{\text{tot}}^z \gg h_{\text{tot}}^x$  as a function of  $\epsilon_0$ . When this requirement is met, then both a phase lapse and an inversion of population are essentially guaranteed to occur. Since  $h_{\text{tot}}^z$  crudely changes by

$$\Delta h_{\text{tot}}^z \sim \frac{2}{\pi}(\Gamma_{\uparrow} - \Gamma_{\downarrow}) \ln(U/\Gamma_{\text{tot}}) \quad (69)$$

as  $\epsilon_0$  is swept across the Coulomb-blockade valley, this leaves us with the criterion

$$(\Gamma_{\uparrow} - \Gamma_{\downarrow}) \ln(U/\Gamma_{\text{tot}}) \gg \sqrt{\Delta^2 + b^2}. \quad (70)$$

Conversely, if  $\sqrt{\Delta^2 + b^2} \gg (\Gamma_{\uparrow} - \Gamma_{\downarrow}) \ln(U/\Gamma_{\text{tot}})$ , then neither a phase lapse nor an inversion of population will occur unless parameters are fine tuned. Thus, the larger  $U$  is, the more ubiquitous phase lapses become.<sup>8,11</sup>

Although the logarithm  $\ln(U/\Gamma_{\text{tot}})$  can be made quite large, in reality we expect it to be a moderate factor of order one. Similarly, the difference in widths  $\Gamma_{\uparrow} - \Gamma_{\downarrow}$  is generally expected to be of comparable magnitude to  $\Gamma_{\uparrow}$ . Under these circumstances, the criterion specified in Eq. (70) reduces to  $\Gamma_{\uparrow} \gg \sqrt{\Delta^2 + b^2}$ . Namely, phase lapses and population inversions are generic as long as the (maximal) tunnelling rate exceeds the level spacing. This conclusion is in line with that of a recent numerical study of multi-level quantum dots.<sup>41</sup>

Finally, we address the effect of nonzero  $h = \sqrt{\Delta^2 + b^2}$  on the correlation-induced resonances. When  $h \gg \Gamma_{\uparrow} \ln(U/\Gamma_{\text{tot}})$ , the effective magnetic field  $h_{\text{tot}} \approx h$  is large throughout the local-moment regime, always exceeding  $\Gamma_{\uparrow}$  and  $\Gamma_{\downarrow}$ . Consequently, the dot is nearly fully polarized for all  $-U < \epsilon_0 < 0$ , and the correlation-induced resonances are washed out. Again, for practical values of  $U/\Gamma_{\text{tot}}$  this regime can equally be characterized by  $h \gg \Gamma_{\uparrow}$ .<sup>11</sup>

The picture for  $\Gamma_{\uparrow} \ln(U/\Gamma_{\text{tot}}) \gg h$  is far more elaborate. When  $T_K|_{\epsilon_0=-U/2} \gg h$ , the magnetic field is uniformly small, and no significant modifications show up as compared with the case where  $h = 0$ . This leaves us with the regime  $T_K|_{\epsilon_0=-U/2} \ll h \ll \Gamma_{\uparrow}$ , where various behaviors can occur. Rather than presenting an exhaustive discussion of this limit, we settle with identifying certain generic features that apply when both components  $|h \cos \theta|$  and  $h \sin \theta$  exceed  $T_K|_{\epsilon_0=-U/2}$ . To begin with, whatever remnants of the correlation-induced resonances that are left, these are shifted away from the middle of the Coulomb-blockade valley in the direction

where  $|h_{\text{tot}}^z|$  acquires its minimal value. Consequently,  $h_{\text{tot}}$  and  $T_K$  no longer obtain their minimal values at the same gate voltage  $\epsilon_0$ . This has the effect of generating highly asymmetric structures in place of the two symmetric resonances that are found for  $h = 0$ . The heights of these features are governed by the “geometric” factors  $\sin^2(\theta_l + s_R \theta_h)$  at the corresponding gate voltages. Their widths are controlled by the underlying Kondo temperatures, which can differ substantially in magnitude. Since the entire structure is shifted away from the middle of the Coulomb-blockade valley where  $T_K$  is minimal, all features are substantially broadened as compared with the correlation-induced resonances for  $h = 0$ . Indeed, similar tendencies are seen in Fig. 5 of Ref.11, even though the model parameters used in this figure lie on the borderline between the mixed-valent and the local-moment regimes.

## VI. CONCLUDING REMARKS

We have presented a comprehensive investigation of the general two-level model for quantum-dot devices. A proper choice of the quantum-mechanical representation of the dot and the lead degrees of freedom reveals an exact mapping onto a generalized Anderson model. In the local-moment regime, the latter Hamiltonian is reduced to an anisotropic Kondo model with a tilted effective magnetic field. As the anisotropic Kondo model flows to the isotropic strong-coupling fixed point, this enables a unified description of all coupling regimes of the original model in terms of the universal magnetization curve of the conventional isotropic Kondo model, for which exact results are available. Various phenomena, such as phase lapses in the transmission phase,<sup>7,8</sup> charge oscillations,<sup>9,10</sup> and correlation-induced resonances<sup>11,12</sup> in the conductance, can thus be accurately and coherently described within a single physical framework.

The enormous reduction in the number of parameters in the system was made possible by the key observation that a general, possibly non-Hermitian tunnelling matrix  $\hat{A}$  can always be diagonalized with the help of two simultaneous unitary transformations, one pertaining the dot degrees of freedom, and the other applied to the lead electrons. This transformation, known as the singular-value decomposition, should have applications in other physical problems involving tunnelling or transfer matrices without any special underlying symmetries.

As the two-level model for transport is quite general, it can potentially be realized in many different ways. As already noted in the main text, the model can be used to describe either a single two-level quantum dot or a double quantum dot where each dot harbors only a single level. Such realizations require that the spin degeneracy of the electrons will be lifted by an external magnetic field. Alternative realizations may directly involve the electron spin. For example, consider a single spinful level coupled to two ferromagnetic leads with *non-collinear* magnetizations. Written in a basis with a particular *ad hoc* local



spin quantization axis, the Hamiltonian of such a system takes the general form of Eq. (1), after properly combining the electronic degrees of freedom in both leads. As is evident from our discussion, the local spin will therefore experience an effective magnetic field that is not aligned with either of the two magnetizations of the leads. This should be contrasted with the simpler configurations of parallel and antiparallel magnetizations, as considered, e.g., in Refs.17,25 and 27.

Another appealing system for the experimental observation of the subtle correlation effects discussed in the present paper is a carbon nanotube-based quantum dot. In such a device both charging energy and single-particle level spacing can be sufficiently large<sup>42</sup> to provide a set of well-separated discrete electron states. Applying external magnetic field either perpendicular<sup>43</sup> or/and parallel<sup>44</sup> to the nanotube gives great flexibility in tuning the energy level structure, and thus turns the system into a valuable testground for probing the Kondo physics addressed in this study.

Throughout this paper we confined ourselves to spinless electrons, assuming that spin degeneracy has been lifted by an external magnetic field. Our mapping can equally be applied to spinful electrons by implementing an identical singular-value decomposition to each of the two spin orientations separately (assuming the tunnelling term is diagonal in and independent of the spin orientation). Indeed, there has been considerable interest lately in spinful variants of the Hamiltonian of Eq. (1), whether in connection with lateral quantum dots,<sup>45,46</sup> capacitively coupled quantum dots,<sup>47,48,49</sup> or carbon nanotube devices.<sup>50</sup> Among the various phenomena that have been discussed in these contexts, let us mention SU(4) variants of the Kondo effect,<sup>47,48,50</sup> and singlet-triplet transitions with two-stage screening on the triplet side.<sup>45,46</sup>

Some of the effects that have been predicted for the spinful case were indeed observed in lateral semiconductor quantum dots<sup>51,52</sup> and in carbon nanotube quantum dots.<sup>44</sup> Still, there remains a distinct gap between the idealized models that have been employed, in which simplified symmetries are often imposed on the tunnelling term, and the actual experimental systems that obviously lack these symmetries. Our mapping should provide a much needed bridge between the idealized models and the actual experimental systems. Similar to the present study, one may expect a single unified description encompassing all coupling regimes in terms of just a few basic low-energy scales. This may provide valuable guidance for analyzing future experiments on such devices.

### Acknowledgments

The authors are thankful to V. Meden for kindly providing the numerical data for the inset in Fig. 6. VK is grateful to Z. A. Németh for stimulating discussions of perturbative calculations. This research was supported by a Center of Excellence of the Israel Science Founda-

tion, and by a grant from the German Federal Ministry of Education and Research (BMBF) within the framework of the German-Israeli Project Cooperation (DIP). We have recently become aware of a related study by Silvestrov and Imry,<sup>53</sup> which independently develops some of the ideas presented in this work.

### APPENDIX A: MAPPING PARAMETERS

In this Appendix we give the details of the mapping of the original Hamiltonian, Eq. (1), onto the generalized Anderson Hamiltonian of Eq. (7).

The first step is the diagonalization of the matrix  $\hat{A}$ , Eq. (6), which describes the coupling between the dot and the leads in the original model. Since  $\hat{A}$  is generally complex and of no particular symmetry, it cannot be diagonalized by a single similarity transformation. Rather, two (generally different) unitary matrices,  $R_d$  and  $R_l$ , are required to achieve a diagonal form,

$$\begin{bmatrix} V_\uparrow & 0 \\ 0 & V_\downarrow \end{bmatrix} = R_l \hat{A} R_d^\dagger. \quad (\text{A1})$$

This representation, known as the singular-value decomposition, is a standard routine in numerical packages. Here we provide a fully analytical treatment of the  $2 \times 2$  case relevant to our discussion. To this end we parametrize the two rotation matrices in the form

$$R_d = e^{i\chi_A} e^{i(\chi_d/2)\tau_z} U(\theta_d, \phi_d), \quad (\text{A2})$$

$$R_l = e^{i(\chi_l/2)\tau_z} U(\theta_l, \phi_l), \quad (\text{A3})$$

where

$$U(\theta, \phi) \equiv \begin{bmatrix} \cos(\theta/2) & e^{-i\phi} \sin(\theta/2) \\ -e^{i\phi} \sin(\theta/2) & \cos(\theta/2) \end{bmatrix} \quad (\text{A4})$$

describes a rotation by angle  $\theta$  about the axis  $-\sin(\phi) \hat{x} + \cos(\phi) \hat{y}$ .

The various parameters that enter Eqs. (A2) and (A3) have simple geometrical interpretations. The two sets of angles,  $(\theta_d, \phi_d)$  and  $(\theta_l, \phi_l)$ , are the longitudinal and the azimuthal angles of the vectors pointing along the direction of the  $z$  axis which defines the corresponding spin variables in Eq. (7), see Fig. 7. The three angles  $\chi_A$ ,  $\chi_d$ , and  $\chi_l$  correspond to the choice of the phases of the single-particle operators  $d_\sigma^\dagger$  and  $c_{k\sigma}^\dagger$ . The latter angles are chosen such that the matrix elements of the transformed Hamiltonian, Eq. (7), will be real with  $h \sin \theta \geq 0$ . Note that  $R_d$  and  $R_l$  are determined up to a common overall phase. This degree of freedom has been exhausted in Eqs. (A2) and (A3) by requiring that  $\det R_l = 1$ .

In order to determine the rotation matrices  $R_d$  and  $R_l$ , one diagonalizes the hermitian matrices  $\hat{A} \hat{A}^\dagger$  and  $\hat{A}^\dagger \hat{A}$ , whose eigenvalues are evidently real and equal to  $|V_\sigma|^2$ . This calculation determines the matrices  $U(\theta_d, \phi_d)$  and

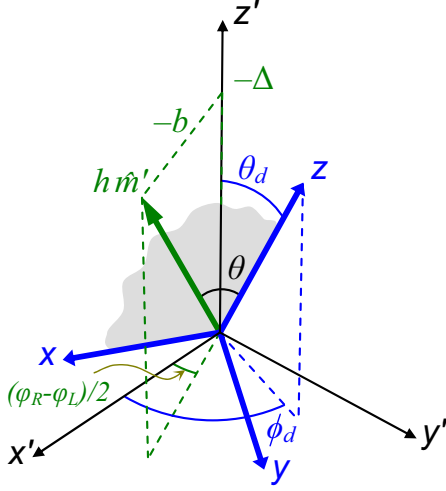


FIG. 7: The original dot degrees of freedom,  $d_1^\dagger$  and  $d_2^\dagger$ , define a pseudo-spin- $\frac{1}{2}$  representation with the axes  $x'$ ,  $y'$ , and  $z'$ . The level indices 1 and 2 are identified in this representation with  $\pm\frac{1}{2}$  spin projections on the  $z'$  axis. The energy splitting  $\Delta$  and the hopping  $b$  combine to define the magnetic-field vector  $h\hat{m}'$ . The unitary matrix  $R_d$  takes the spin to a new coordinate system whose axes are labelled with  $x$ ,  $y$ , and  $z$ . The new “spin” labels  $\sigma = \uparrow$  and  $\sigma = \downarrow$  represent  $\pm\frac{1}{2}$  spin projections on the new  $z$  axis, whose direction is defined by the longitudinal and the azimuthal angles  $\theta_d$  and  $\phi_d$ . The new  $x$  axis lies in the plane of vectors  $\hat{z}$  and  $h\hat{m}'$ . A similar picture applies to the conduction-electron degrees of freedom, where the lead index  $\alpha = L, R$  plays the same role as the original level index  $i = 1, 2$ .

$U(\theta_l, \phi_l)$ , and yields the values of  $|V_\sigma|$ . Indeed, using Eqs. (A1), (A2), and (A3), one obtains

$$\begin{aligned} \begin{bmatrix} |V_\uparrow|^2 & 0 \\ 0 & |V_\downarrow|^2 \end{bmatrix} &= U(\theta_l, \phi_l) \hat{A} \hat{A}^\dagger U^\dagger(\theta_l, \phi_l) \\ &= U(\theta_d, \phi_d) \hat{A}^\dagger \hat{A} U^\dagger(\theta_d, \phi_d). \end{aligned} \quad (\text{A5})$$

Assuming  $|V_\uparrow| > |V_\downarrow|$  (the case where  $|V_\uparrow| = |V_\downarrow|$  is treated separately in Sec. A2), these two equations give

$$|V_\sigma|^2 = X \pm Y, \quad (\text{A6})$$

$$\theta_{d/l} = 2 \arctan \sqrt{\frac{Y - Z_{d/l}}{Y + Z_{d/l}}}, \quad (\text{A7})$$

$$\phi_d = \arctan \left( \frac{a_{L1}a_{L2} - a_{R1}a_{R2}}{a_{L1}a_{L2} + a_{R1}a_{R2}} \tan \frac{\varphi}{2} \right) + \pi \eta_d, \quad (\text{A8})$$

$$\phi_l = \arctan \left( \frac{a_{L2}a_{R2} - a_{L1}a_{R1}}{a_{L2}a_{R2} + a_{L1}a_{R1}} \tan \frac{\varphi}{2} \right) + \pi \eta_l, \quad (\text{A9})$$

where

$$X = \frac{1}{2} \sum_{\alpha i} a_{\alpha i}^2, \quad (\text{A10})$$

$$Y = \sqrt{X^2 - |\det \hat{A}|^2}, \quad (\text{A11})$$

$$Z_d = \frac{1}{2} \sum_{\alpha=L,R} (a_{\alpha 1}^2 - a_{\alpha 2}^2), \quad (\text{A12})$$

$$Z_l = \frac{1}{2} \sum_{i=1,2} (a_{Li}^2 - a_{Ri}^2), \quad (\text{A13})$$

and

$$2\eta_d = 1 - \text{sgn} \left[ (a_{L1}a_{L2} + a_{R1}a_{R2}) \cos \frac{\varphi}{2} \right], \quad (\text{A14})$$

$$2\eta_l = 1 - \text{sgn} \left[ (a_{L1}a_{R1} + a_{L2}a_{R2}) \cos \frac{\varphi}{2} \right]. \quad (\text{A15})$$

The plus sign in Eq. (A6) corresponds to  $V_\uparrow$ , since the spin-up direction is defined as the one with the larger coupling,  $|V_\uparrow|^2 > |V_\downarrow|^2$ . The longitudinal angles  $0 \leq \theta_d, \theta_l \leq \pi$  are uniquely defined by Eq. (A7), while the quadrants for the azimuthal angles  $-\pi/2 < \phi_d, \phi_l \leq 3\pi/2$  must be chosen according to Eqs. (A14) and (A15). The auxiliary quantities in Eqs. (A10)–(A13) obey the inequalities  $X \geq Y$  and  $Y \geq |Z_{d/l}|$ .

The next step is to determine the angles  $\chi_A$ ,  $\chi_d$ , and  $\chi_l$  which come to assure, among other things, that  $V_\uparrow > V_\downarrow$  are both real and non-negative. Let us begin with  $\chi_A$ . When  $\det \hat{A} \neq 0$ , i.e., for  $V_\downarrow > 0$ , the angle  $\chi_A$  is uniquely determined by taking the determinants of both sides of Eq. (A1) and equating their arguments. This yields

$$\chi_A = \frac{1}{2} \arg \det \hat{A}. \quad (\text{A16})$$

When  $\det \hat{A} = 0$ , the angle  $\chi_A$  can take arbitrary values. This stems from the fact that  $V_\downarrow = 0$ , and therefore  $c_{k\downarrow}$  can be attached an arbitrary phase without affecting the form of Eq. (7). In this case we choose  $\chi_A = 0$ .

Next we rotate the Hamiltonian term  $\hat{\mathcal{E}}_d$ , which is the first term of the isolated dot Hamiltonian, Eq. (3). Upon converting to the rotated dot operators  $d_\uparrow^\dagger$  and  $d_\downarrow^\dagger$ , the single-particle term  $\hat{\mathcal{E}}_d$  transforms according to

$$\hat{\mathcal{E}}_d \rightarrow R_d \hat{\mathcal{E}}_d R_d^\dagger. \quad (\text{A17})$$

Consider first the partial rotation  $U(\theta_d, \phi_d) \hat{\mathcal{E}}_d U^\dagger(\theta_d, \phi_d)$  [see Eq. (A2)]. Writing  $\hat{\mathcal{E}}_d$  [as defined in Eq. (4)] in the form

$$\hat{\mathcal{E}}_d = \epsilon_0 - \frac{h}{2} \hat{m}' \cdot \vec{\tau} \quad (\text{A18})$$

with

$$h = \sqrt{\Delta^2 + b^2} \quad (\text{A19})$$

and

$$\hat{m}' = -\frac{b}{h} \cos \frac{\varphi_L - \varphi_R}{2} \hat{x} + \frac{b}{h} \sin \frac{\varphi_L - \varphi_R}{2} \hat{y} - \frac{\Delta}{h} \hat{z}, \quad (\text{A20})$$

the partial rotation  $U(\theta_d, \phi_d) \hat{\mathcal{E}}_d U^\dagger(\theta_d, \phi_d)$  gives

$$\epsilon_0 - \frac{h}{2} \hat{m} \cdot \vec{\tau}, \quad (\text{A21})$$

where  $\hat{m}$  is the unit vector obtained by rotating  $\hat{m}'$  by an angle  $-\theta_d$  about the axis  $-\sin(\phi_d) \hat{x} + \cos(\phi_d) \hat{y}$ . Defining the angle  $\theta \in [0, \pi]$  which appears in Eq. (7) according to  $\cos \theta = m_z$ , it follows from simple geometry that

$$\begin{aligned} \cos \theta &= -\frac{\Delta}{h} \cos \theta_d \\ &- \frac{b}{h} \sin \theta_d \cos[\phi_d + (\varphi_L - \varphi_R)/2]. \end{aligned} \quad (\text{A22})$$

The full transformation  $R_d \hat{\mathcal{E}}_d R_d^\dagger$  corresponds to yet another rotation of  $\hat{m}$  by an angle  $-\chi_d$  about the  $z$  axis. The angle  $\chi_d$  is chosen such that the projection of  $\hat{m}$  onto the  $xy$  plane is brought to coincide with the  $x$  direction. This fixes  $\chi_d$  uniquely, unless  $h \sin \theta$  happens to be zero (whether because  $h = 0$  or because  $\theta$  is an integer multiple of  $\pi$ ). When  $h \sin \theta = 0$ , the angle  $\chi_d$  can take arbitrary values. Physically this stems from the fact that spin-up and spin-down degrees of freedom can be gauged separately within Eq. (7). We choose  $\chi_d = 0$  in this case. The explicit expression for  $\chi_d$  when  $h \sin \theta \neq 0$  is quite cumbersome and will not be specified. As for the remaining angle  $\chi_l$ , it is fixed by the requirement that  $V_\sigma$  will be real and non-negative.

Note that the conditions for the two exactly solvable cases quoted in the main text, Eqs. (10) and (11), are readily derived from our expressions for the eigenvalues  $V_\sigma$ . The first case, Eq. (10), corresponds to  $V_\downarrow = 0$ , which requires  $\det \hat{A} = e^{i\varphi} a_{L1} a_{R2} - a_{L2} a_{R1} = 0$ . This immediately leads to Eq. (10). The second solvable case, Eq. (11), corresponds to equal eigenvalues, which implies  $Y = 0$  [Eqs. (A6), (A10) and (A11) remain intact for  $|V_\uparrow| = |V_\downarrow|$ ]. By virtue of the inequalities  $Y \geq |Z_{d/l}|$ , this necessitates that  $Z_d$  and  $Z_l$  are both zero, which gives rise to the first two conditions in Eq. (11). The remaining condition on the Aharonov-Bohm phase  $\varphi$  follows from substituting the first two conditions into the definition of  $Y$  and equating  $Y$  to zero.

### 1. No Aharonov-Bohm fluxes

Of particular interest is the case where no Aharonov-Bohm fluxes are present,  $\varphi_L = \varphi_R = 0$ . In the absence of a real magnetic field that penetrates the structure, the parameters that appear in the Hamiltonian of Eq. (1) are all real. This greatly simplifies the resulting expressions for the rotation matrices  $R_d$  and  $R_l$ , as well as for the model parameters that appear in Eq. (7). In this subsection, we provide explicit expression for these quantities in the absence of Aharonov-Bohm fluxes, focusing on the case where  $V_\uparrow > V_\downarrow$ . The case where  $V_\uparrow = V_\downarrow$  is treated separately in Sec. A 2.

As is evident from Eqs. (A8) and (A9), each of the azimuthal angles  $\phi_d$  and  $\phi_l$  is either equal to 0 or  $\pi$  when  $\varphi = 0$ . (The corresponding  $y'$  and  $y$  axes are parallel in Fig. 7.) It is therefore advantageous to set both azimuthal angles to zero at the expense of extending the range for the longitudinal angles  $\theta_d$  and  $\theta_l$  from  $[0, \pi]$  to  $(-\pi, \pi]$ . Within this convention, Eq. (A7) is replaced with

$$\theta_{d/l} = 2 s_{d/l} \arctan \sqrt{\frac{Y - Z_{d/l}}{Y + Z_{d/l}}}, \quad (\text{A23})$$

where

$$s_d = \text{sgn}(a_{L1} a_{L2} + a_{R1} a_{R2}), \quad (\text{A24})$$

$$s_l = \text{sgn}(a_{L1} a_{R1} + a_{L2} a_{R2}). \quad (\text{A25})$$

Similarly, the unit vector  $\hat{m}'$  of Eq. (A20) reduces to

$$\hat{m}' = -\frac{b}{h} \hat{x} - \frac{\Delta}{h} \hat{z}, \quad (\text{A26})$$

which results in

$$\begin{aligned} \hat{m} &= \left[ -\frac{b}{h} \cos \theta_d + \frac{\Delta}{h} \sin \theta_d \right] \hat{x} \\ &- \left[ \frac{b}{h} \sin \theta_d + \frac{\Delta}{h} \cos \theta_d \right] \hat{z} \end{aligned} \quad (\text{A27})$$

and

$$\theta = \pi - \arccos \left( \frac{b}{h} \sin \theta_d + \frac{\Delta}{h} \cos \theta_d \right). \quad (\text{A28})$$

Since the rotated unit vector  $\hat{m}$  has no  $y$  component, the angle  $\chi_d$  is either equal to 0 or  $\pi$ , depending on the sign of  $m_x$ . Assuming  $\det \hat{A} \neq 0$  and using Eqs. (A4) and (A16), one can write Eq. (A2) in the form

$$R_d = (\text{sgn} \det \hat{A})^{1/2} e^{i\pi(1-s_\theta)\tau_z/4} e^{i(\theta_d/2)\tau_y}, \quad (\text{A29})$$

$$s_\theta = \text{sgn} m_x = \text{sgn}(\Delta \sin \theta_d - b \cos \theta_d). \quad (\text{A30})$$

Note that the first exponent in Eq. (A29) is equal to 1 for  $s_\theta = +1$ , and is equal to  $e^{i(\pi/2)\tau_z}$  for  $s_\theta = -1$ . If  $\det \hat{A} = 0$  we set  $\text{sgn} \det \hat{A} \rightarrow 1$  in Eq. (A29), while for  $\Delta \sin \theta_d = b \cos \theta_d$  we select  $s_\theta = +1$ .

Proceeding to the remaining angle  $\chi_l$ , we note that  $R_d$  of Eq. (A29) is either purely real or purely imaginary, depending on whether

$$s_R = s_\theta \text{sgn} \det \hat{A} \quad (\text{A31})$$

is positive or negative. Since both  $e^{i(\theta_l/2)\tau_y}$  and  $\hat{A}$  are real matrices, then  $e^{i(\chi_l/2)\tau_z}$  must also be either purely real or purely imaginary in tandem with  $R_d$  in order for the eigenvalues  $V_\uparrow$  and  $V_\downarrow$  to be real. This consideration dictates that  $\chi_l$  is an integer multiple of  $\pi$ , with an even (odd) integer for positive (negative)  $s_R$ . The end result for  $R_l$  is therefore

$$R_l = \eta_R e^{i\pi(1-s_R)\tau_z/4} e^{i(\theta_l/2)\tau_y}, \quad (\text{A32})$$

Here  $\eta_R = \pm 1$  is an overall phase which comes to assure that the eigenvalues  $V_\uparrow$  and  $V_\downarrow$  are non-negative.

## 2. Isotropic couplings, $V_\uparrow = V_\downarrow$

Our general construction of the rotation matrices  $R_d$  and  $R_l$  fails when  $|V_\uparrow| = |V_\downarrow| = V$ . Equations (A6), (A10) and (A11) remain in tact for  $|V_\uparrow| = |V_\downarrow|$ , however the angles  $\theta_{d/l}$  and  $\phi_{d/l}$  are ill-defined in Eqs. (A7)–(A9). This reflects the fact that the matrices  $\hat{A}^\dagger \hat{A}$  and  $\hat{A} \hat{A}^\dagger$  are both equal to  $V^2$  times the unit matrix, hence any rotation matrix  $U(\theta, \phi)$  can be used to “diagonalize” them. There are two alternatives for treating the isotropic case where  $|V_\uparrow| = |V_\downarrow|$ . The first possibility is to add an infinitesimal matrix  $\eta \hat{B}$  that lifts the degeneracy of  $|V_\uparrow|$  and  $|V_\downarrow|$ :  $\hat{A} \rightarrow \hat{A} + \eta \hat{B}$ . Using the general construction outlined above and implementing the limit  $\eta \rightarrow 0$ , a proper pair of rotation matrices  $R_d$  and  $R_l$  are obtained. The other alternative is to directly construct the rotation matrices  $R_d$  and  $R_l$  pertaining to this case. Below we present this second alternative.

A key observation for the isotropic case pertains to the “reduced” matrix

$$\hat{T} = (\det \hat{A})^{-1/2} \hat{A}, \quad (\text{A33})$$

which obeys

$$\hat{T}^\dagger \hat{T} = \hat{T} \hat{T}^\dagger = 1, \quad \det \hat{T} = 1. \quad (\text{A34})$$

As a member of the SU(2) group,  $\hat{T}$  can be written in the form

$$\hat{T} = U(\theta_T, \phi_T) e^{i(\chi_T/2)\tau_z} \quad (\text{A35})$$

with  $\theta_T \in [0, \pi]$ . Explicitly, the angles  $\theta_T$ ,  $\phi_T$  and  $\chi_T$  are given by

$$\theta_T = 2 \arccos(|\det \hat{A}|^{-1/2} |a_{L1}|), \quad (\text{A36})$$

$$\chi_T = 2 \arg[(\det \hat{A})^{-1/2} a_{L1}], \quad (\text{A37})$$

and

$$\phi_T = \arg[(\det \hat{A})^{-1/2} a_{R1}] - \pi - \chi_T/2. \quad (\text{A38})$$

Exploiting the fact that  $\det \hat{A} = V^2$ , the matrix  $\hat{A}$  takes then the form

$$\hat{A} = V R_l^\dagger R_d = V e^{i\chi_A} U(\theta_T, \phi_T) e^{i(\chi_T/2)\tau_z}, \quad (\text{A39})$$

where the angle  $\chi_A$  is defined in Eq. (A16).

Equation (A39) determines the matrix product  $R_l^\dagger R_d$ . Any two rotation matrices that satisfy the right-most equality in Eq. (A39) transform the tunnelling matrix  $\hat{A}$  to  $V$  times the unit matrix, as is required. The rotation matrix  $R_d$  is subject to yet another constraint, which stems from the requirement that  $h \sin \theta \geq 0$  in Eq. (7). We note that this constraint as well does not uniquely determine the matrix  $R_d$ .<sup>30</sup> Perhaps the simplest choice for  $R_d$  is given by

$$R_d = e^{i\chi_A} e^{i(\chi_d/2)\tau_z} \quad (\text{A40})$$

with

$$\chi_d = \frac{1}{2}(\varphi_L - \varphi_R) + \frac{\pi}{2}(1 - \text{sgn } b), \quad (\text{A41})$$

which corresponds to

$$h \cos \theta = -\Delta, \quad h \sin \theta = |b|. \quad (\text{A42})$$

Adopting the choice of Eq. (A40), the rotation matrix  $R_l$  takes the form

$$R_l = e^{i\tau_z(\chi_d - \chi_T)/2} U(\theta_T, -\phi_T), \quad (\text{A43})$$

where  $\theta_T$ ,  $\phi_T$ ,  $\chi_T$  and  $\chi_d$  are listed above.

## APPENDIX B: BETHE ANSATZ FORMULAE

In this appendix we gather for convenience all relevant details of the exact Bethe *ansatz* solutions for the impurity magnetization in the isotropic Kondo and Anderson models in the presence of a finite magnetic field. Extensive reviews of these solutions (including the anisotropic Kondo model) are available in the literature.<sup>19,20,22</sup> Here we only summarize the main results of relevance to our analysis, and briefly comment on the numerical procedure. We confine ourselves to zero temperature, although explicit equations do exist also at finite temperature. Throughout the Appendix we employ units in which  $\mu_{BG} = 1$ .

### 1. Isotropic Kondo model

We begin the presentation with the case of a Kondo impurity, before turning to the more elaborate case of an Anderson impurity. As a function of the magnetic field  $h$ , the magnetization of an isotropic spin- $\frac{1}{2}$  Kondo impurity is given by the explicit expression [see, e.g., Eq. (6.23) of Ref.22]

$$M(h) = \frac{-i}{4\sqrt{\pi}} \int_{-\infty}^{+\infty} d\omega \frac{(i\omega + 0)^{i\omega/2\pi} \text{sech}(\frac{\omega}{2})}{(\omega - i0)\Gamma(\frac{1}{2} + i\frac{\omega}{2\pi})} \left(\frac{h}{2\pi T_K}\right)^{i\omega/\pi}. \quad (\text{B1})$$

Here  $\Gamma(z)$  is the complex gamma function. The Kondo temperature,  $T_K$ , is defined via the inverse of the spin susceptibility,

$$T_K^{-1} \equiv 2\pi \lim_{h \rightarrow 0} M(h)/h. \quad (\text{B2})$$

Evidently, Eq. (B1) is a universal function of the ratio  $h/T_K$ , which is denoted in the main text by  $M_K(h/T_K)$ . It has the asymptotic expansion

$$M(h) \simeq \begin{cases} h/(2\pi T_K), & h \ll T_K, \\ \frac{1}{2} - \frac{1}{4 \ln(h/T_H)} - \frac{\ln \ln(h/T_H)}{8 \ln^2(h/T_H)}, & h \gg T_K, \end{cases} \quad (\text{B3})$$

where  $T_H \equiv \sqrt{\pi/e} T_K$ .

## 2. Isotropic Anderson model

In contrast to the Kondo model, there are no closed-form expressions for the total impurity occupancy  $n_{\text{tot}} = \langle n_{\uparrow} + n_{\downarrow} \rangle$  and magnetization  $M = \langle n_{\uparrow} - n_{\downarrow} \rangle / 2$  in the isotropic Anderson model. The exact Bethe *ansatz* solution of the model provides a set of coupled linear integral equations from which  $n_{\text{tot}}$  and  $M$  can be computed. Below we summarize the equations involved and comment on the numerical procedure that is required for solving these equations. The expressions detailed below apply to arbitrary  $\epsilon_0$ ,  $U$ ,  $h$ , and  $\Gamma$  at zero temperature. In terms of the Hamiltonian of Eq. (7), we restrict the discussion to  $\Gamma = \Gamma_{\uparrow} = \Gamma_{\downarrow}$  (isotropic Anderson model) and  $\sin \theta = 0$  (parallel-field configuration). The case  $\sin \theta \neq 0$  follows straightforwardly from a simple rotation of the dot and the conduction-electron operators about the  $y$  axis.

### a. Kondo temperature

The most accurate analytical expression that is available for the Kondo temperature of the isotropic Anderson model can be written as

$$T_K = (\sqrt{2U\Gamma}/\pi) \exp[\pi(\Gamma^2 + \epsilon_0 U + \epsilon_0^2)/(2U\Gamma)], \quad (\text{B4})$$

where  $\Gamma = \pi\rho|V|^2$ . This expression for  $T_K$  exactly reproduces Eq. (6.22) of Ref.22 for the symmetric Anderson model,  $\epsilon_0 = -U/2$ . It also coincides with Eq. (7.11) of Ref.22 for the Kondo temperature of the asymmetric model when  $U \gg \Gamma$ . Note that the  $\Gamma^2$  term in the exponent is usually omitted from Eq. (B4) on the basis of it being small. It does in general improve the estimate for  $T_K$ .

In the local-moment regime, where Eq. (B4) is valid, the impurity magnetization of the isotropic Anderson model is dominated by the universal magnetization curve of Eq. (B1) up to fields of the order of  $h \sim \sqrt{\Gamma U} \gg T_K$  (see, e.g., lower left inset to Fig. 2). At yet larger fields,  $h \gg \sqrt{\Gamma U}$ , the magnetization of the Anderson model can

no longer be described by that of the Kondo model, as charge fluctuations become exceedingly more important than spin flips. Rather,  $M$  is well described by perturbation theory in  $\Gamma$ . Importantly, the asymptotic expansion of Eq. (B3) properly matches (to leading order in  $\Gamma/U$ ) the perturbative result<sup>9</sup> for  $M$  when  $h \sim \sqrt{\Gamma U}$ . Thus, the two approaches combine to cover the entire range in  $h$  for the Anderson model.

### b. Bethe ansatz equations for the occupancy and magnetization

The Bethe *ansatz* solution of the Anderson model features four key quantities, which are the distributions of the charge and spin rapidities,  $\tilde{\rho}_{i/h}(k)$  and  $\tilde{\sigma}_{i/h}(\lambda)$ , respectively, for the impurity ( $i$ ) and the host ( $h$ ) band. The total impurity occupancy and magnetization are expressed as integrals over the distributions of the charge and spin rapidities for the impurity:

$$M = \frac{1}{2} \int_{-\infty}^B \tilde{\rho}_i(k) dk, \quad (\text{B5})$$

$$n_d = 1 - \int_{-\infty}^Q \tilde{\sigma}_i(\lambda) d\lambda. \quad (\text{B6})$$

The upper limits of integration in Eqs. (B5) and (B6) are determined through implicit conditions on the corresponding distribution functions for the host band,

$$\frac{h}{2\pi} = \int_{-\infty}^B \tilde{\rho}_h(k) dk, \quad (\text{B7})$$

$$\frac{U + 2\epsilon_0}{2\pi} = \int_{-\infty}^Q \tilde{\sigma}_h(\lambda) d\lambda. \quad (\text{B8})$$

As for the distributions of the rapidities for the impurity and the host, these are determined by the same pair of linear integral equations, only with different inhomogeneous parts:

$$\tilde{\rho}(k) + \frac{dg(k)}{dk} \int_{-\infty}^B R[g(k) - g(k')] \tilde{\rho}(k') dk' + \frac{dg(k)}{dk} \int_{-\infty}^Q S[g(k) - \lambda] \tilde{\sigma}(\lambda) d\lambda = \tilde{\rho}^{(0)}(k), \quad (\text{B9})$$

$$\tilde{\sigma}(\lambda) - \int_{-\infty}^Q R[\lambda - \lambda'] \tilde{\sigma}(\lambda') d\lambda' + \int_{-\infty}^B S[\lambda - g(k)] \tilde{\rho}(k) dk = \tilde{\sigma}^{(0)}(\lambda), \quad (\text{B10})$$

where<sup>54</sup>

$$S(x) = \frac{1}{2 \cosh(\pi x)}, \quad (\text{B11})$$

$$R(x) = \frac{1}{2\pi} \text{Re} \left[ \Psi \left( 1 + i \frac{x}{2} \right) - \Psi \left( \frac{1}{2} + i \frac{x}{2} \right) \right], \quad (\text{B12})$$

$$g(k) = \frac{(k - \epsilon_0 - U/2)^2}{2U\Gamma} \quad (\text{B13})$$

(here  $\Psi$  is the digamma function). The inhomogeneous

parts in Eqs. (B9) and (B10) are given in turn by

$$\tilde{\rho}_i^{(0)}(k) = \tilde{\Delta}(k) + \frac{dg(k)}{dk} \int_{-\infty}^{+\infty} R[g(k) - g(k')] \tilde{\Delta}(k') dk', \quad (\text{B14})$$

$$\tilde{\rho}_h^{(0)}(k) = \frac{1}{2\pi} \left\{ 1 + \frac{dg(k)}{dk} \int_{-\infty}^{+\infty} R[g(k) - g(k')] dk' \right\}, \quad (\text{B15})$$

$$\tilde{\sigma}_i^{(0)}(\lambda) = \int_{-\infty}^{+\infty} S[\lambda - g(k)] \tilde{\Delta}(k) dk, \quad (\text{B16})$$

$$\tilde{\sigma}_h^{(0)}(\lambda) = \frac{1}{2\pi} \int_{-\infty}^{+\infty} S[\lambda - g(k)] dk, \quad (\text{B17})$$

where  $\tilde{\Delta}(k)$  is the Lorentzian function

$$\tilde{\Delta}(k) = \frac{1}{\pi} \frac{\Gamma}{\Gamma^2 + (k - \epsilon_0)^2}. \quad (\text{B18})$$

### c. Details of the numerical procedure

The main obstacle faced with in a numerical solution of the Bethe *ansatz* equations is the self-consistent determination of the upper integration bounds that appear in Eqs. (B5)–(B10). These are computed iteratively according to the scheme

$$\tilde{\rho}_h^{(n-1)}, \tilde{\sigma}_h^{(n-1)} \Rightarrow B^{(n)}, Q^{(n)} \Rightarrow \tilde{\rho}_h^{(n)}, \tilde{\sigma}_h^{(n)}. \quad (\text{B19})$$

Starting with  $\tilde{\rho}_h^{(n-1)}$  and  $\tilde{\sigma}_h^{(n-1)}$  as input for the  $n$ th iteration,  $B^{(n)}$  and  $Q^{(n)}$  are extracted from Eqs. (B7) and

(B8). Using the updated values for  $B$  and  $Q$ ,  $\tilde{\rho}_h^{(n)}(k)$  and  $\tilde{\sigma}_h^{(n)}(\lambda)$  are then obtained from the solution of Eqs. (B9) and (B10). This cycle is repeated until convergence is reached. The first iteration in this procedure is usually initialized with  $\tilde{\rho}_h^{(0)}(k)$  and  $\tilde{\sigma}_h^{(0)}(\lambda)$  as input. Standard techniques are then used to ensure rapid convergence of the iterative solution. Typically 15 to 30 iterations are required to achieve a relative accuracy of  $10^{-4}$  for the vector  $(B, Q)$ .

The core of this cycle is the solution of Eqs. (B9) and (B10). These are solved (for given values of  $B$  and  $Q$ ) by discretizing the integration interval with adaptively chosen  $500 \div 1000$  mesh points. Once a self-consistent solution is reached for  $B$ ,  $Q$ ,  $\tilde{\rho}_h(k)$  and  $\tilde{\sigma}_h(\lambda)$ , the corresponding distributions of rapidities for the impurity are obtained from a single solution of Eqs. (B9) and (B10). The impurity occupancy and magnetization are calculated in turn from Eqs. (B5) and (B6).

To test the accuracy of our numerical results, we have extensively checked them against the analytical solution for the zero-field occupancy  $n_d(h=0)$  and the zero-field susceptibility  $dM/dh|_{h=0}$ . In suitable parameter regimes, we have also compared our results to perturbation theory in both  $U$  and  $\Gamma$ . In all cases tested the relative errors in  $n_d$  and  $M$  were less than 0.05% and 0.5%, respectively. This accuracy can be systematically improved by increasing the number of discretization points used in solving Eqs. (B9) and (B10) for the distributions. Our results were also in full agreement with those reported by Okiji and Kawasaki,<sup>23</sup> except for  $M(h)$  where up to 10% differences were found. Considering the extensive set of checks that were applied to our results, it appears that the discrepancy is due to lower numerical accuracy in the solution of Ref. 23.

---

\* Electronic address: slava@latnet.lv

<sup>1</sup> P. W. Anderson, Phys. Rev. **124**, 41 (1961).

<sup>2</sup> T. K. Ng and P. A. Lee, Phys. Rev. Lett. **61**, 1768 (1988).

<sup>3</sup> L. I. Glazman and M. E. Raikh, Pis'ma Zh. Eksp. Teor. Fiz. **47**, 378 (1988), [JETP Lett. **47**, 452 (1988)].

<sup>4</sup> D. Goldhaber-Gordon, J. Göres, M. A. Kastner, H. Shtrikman, D. Mahalu, and U. Meirav, Phys. Rev. Lett. **81**, 5225 (1998).

<sup>5</sup> W. G. van der Wiel, S. De Franceschi, T. Fujisawa, J. M. Elzerman, S. Tarucha, and L. P. Kouwenhoven, Science **289**, 2105 (2000).

<sup>6</sup> D. Boese, W. Hofstetter, and H. Schoeller, Phys. Rev. B **64**, 125309 (2001).

<sup>7</sup> A. Silva, Y. Oreg, and Y. Gefen, Phys. Rev. B **66**, 195316 (2002).

<sup>8</sup> D. I. Golosov and Y. Gefen (2006), unpublished, cond-mat/0601342.

<sup>9</sup> J. König and Y. Gefen, Phys. Rev. B **71**, 201308(R) (2005).

<sup>10</sup> M. Sindel, A. Silva, Y. Oreg, and J. von Delft, Phys. Rev. B **72**, 125316 (2005).

<sup>11</sup> V. Meden and F. Marquardt, Phys. Rev. Lett. **96**, 146801

(2006).

<sup>12</sup> C. Karrasch, T. Enss, and V. Meden, Phys. Rev. B **73**, 235337 (2006).

<sup>13</sup> P. G. Silvestrov and Y. Imry, Phys. Rev. Lett. **85**, 2565 (2000).

<sup>14</sup> F. D. M. Haldane, Phys. Rev. Lett. **40**, 416 (1978).

<sup>15</sup> J. R. Schrieffer and P. A. Wolff, Phys. Rev. **149**, 491 (1966).

<sup>16</sup> P. W. Anderson, J. Phys. C **3**, 2436 (1970).

<sup>17</sup> J. Martinek, Y. Utsumi, H. Imamura, J. Barnaś, S. Maekawa, J. König, and G. Schön, Phys. Rev. Lett. **91**, 127203 (2003).

<sup>18</sup> P. W. Anderson, G. Yuval, and D. R. Hamann, Phys. Rev. B **1**, 4464 (1970).

<sup>19</sup> N. Andrei, K. Furuya, and J. H. Lowenstein, Rev. Mod. Phys. **55**, 331 (1983).

<sup>20</sup> A. M. Tselick and P. B. Wiegmann, Adv. Phys. **32**, 453 (1983).

<sup>21</sup> D. C. Langreth, Phys. Rev. **150**, 516 (1966).

<sup>22</sup> P. B. Wiegmann and A. M. Tselick, J. Phys. C **16**, 2281 (1983).

- <sup>23</sup> A. Okiji and N. Kawakami, J. Phys. Soc. Jpn. **51**, 3192 (1982).
- <sup>24</sup> Assigning the same density of states,  $\rho$ , to both leads does not restrict the generality of our model, since the case of  $\rho_L \neq \rho_R$  can be accounted for by an appropriate rescaling of the tunnelling matrix  $\hat{A}$ .
- <sup>25</sup> J. Martinek, M. Sindel, L. Borda, J. Barnaś, J. König, G. Schön, and J. von Delft, Phys. Rev. Lett. **91**, 247202 (2003).
- <sup>26</sup> A. N. Pasupathy, R. C. Bialczak, J. Martinek, J. E. Grose, L. A. K. Donev, P. L. McEuen, and D. C. Ralph, Science **306**, 86 (2004).
- <sup>27</sup> J. Martinek, M. Sindel, L. Borda, J. Barnaś, R. Bulla, J. König, G. Schön, S. Maekawa, and J. von Delft, Phys. Rev. B **72**, 121302(R) (2005).
- <sup>28</sup> For ferromagnetic leads, the conduction-electron density of states,  $\rho_\sigma$ , is spin dependent, which can be converted into spin-dependent tunnelling amplitudes  $V_\sigma$  by appropriate rescaling.
- <sup>29</sup> G. H. Golub and C. F. Van Loan, *Matrix Computations* (Johns Hopkins University Press, Baltimore, MD, 1996), pp. 70–71, 3rd ed.
- <sup>30</sup> If either  $\det \hat{A} = 0$ ,  $h \sin \theta = 0$ , or  $V_\uparrow = V_\downarrow$ , then there is an additional degree of freedom in constructing the unitary matrices  $R_l$  and  $R_d$ . As detailed in Appendix A, when  $\det \hat{A} = 0$  the angle  $\chi_A$  can take arbitrary values, while for  $h \sin \theta = 0$  the angle  $\chi_d$  can be arbitrary [see Eqs. (A2) and (A3) for the definitions of these angles]. If  $V_\uparrow = V_\downarrow$ , then the angle  $\theta$  can take any value in the range  $0 \leq \theta \leq \pi$ .
- <sup>31</sup> M. Pustilnik and L. I. Glazman, Phys. Rev. B **64**, 045328 (2001).
- <sup>32</sup> The phase  $\varphi$  is ill-defined when any of the coefficients  $a_{L1}$ ,  $a_{L2}$ ,  $a_{R1}$ , and  $a_{R2}$  is zero.
- <sup>33</sup> Note that the Friedel-Langreth sum rule was derived for the Anderson impurity model rather than the Kondo model.
- <sup>34</sup> The universal function  $M_K(h/T_K)$  pertains, strictly speaking, to a global magnetic field that couples simultaneously to the impurity and the conduction electrons with equal  $g$ -factors. Here, by contrast, one is dealing with a local magnetic field that couples solely to the impurity. However, in the scaling regime of interest here, the impurity magnetization is the same for a local and a global magnetic field.
- <sup>35</sup> Formally, these corrections to the dot charge follow quantitatively from the fact that, when properly transformed under the Schrieffer-Wolff transformation, the local dot operators  $d_\sigma^\dagger$  are slightly mixed with the conduction-electron degrees of freedom. Note also that to first order in  $\Gamma_\alpha$  the total charge  $n_{\text{tot}}$  is independent of basis rotation.
- <sup>36</sup> Only small nonmonotonicities in the charging are reported in the nonperturbative numerical renormalization-group calculations of Ref.10 for  $\Gamma_\uparrow = \Gamma_\downarrow$ . The regime of nearly degenerate levels, which is required for the appearance of the large feature reported here, has not been studied in Ref.10.
- <sup>37</sup> The improved fRG data for the inset have been kindly provided to us by V. Meden.
- <sup>38</sup> K. G. Wilson, Rev. Mod. Phys. **47**, 773 (1975).
- <sup>39</sup> For the special case where  $a_{L1} = a_{R1}$  and  $a_{L2} = -a_{R2}$ , our  $\Gamma_\uparrow$  and  $\Gamma_\downarrow$  are related to those of Ref.11 though  $\Gamma_\uparrow = 2 \max\{\Gamma_1^L, \Gamma_2^L\}$  and  $\Gamma_\downarrow = 2 \min\{\Gamma_1^L, \Gamma_2^L\}$ .
- <sup>40</sup> Here we have neglected exponentially small corrections of order  $\Gamma_{\text{tot}} \delta \epsilon_{\text{CIR}} / U^2$  to the total dot occupancy. These stem from the fact that  $\epsilon_0$  is slightly removed from the middle of the Coulomb-blockade valley, i.e.,  $\epsilon_0 \rightarrow \pm \delta \epsilon_{\text{CIR}}$  in Eq. (50).
- <sup>41</sup> C. Karrasch, T. Hecht, Y. Oreg, J. von Delft, and V. Meden (2006), unpublished, cond-mat/0609191.
- <sup>42</sup> M. R. Buitelaar, A. Bachtold, T. Nussbaumer, M. Iqbal, and C. Schönenberger, Phys. Rev. Lett. **88**, 156801 (2002).
- <sup>43</sup> J. Nygård, D. H. Cobden, and P. E. Lindelof, Nature **408**, 342 (2000).
- <sup>44</sup> P. Jarillo-Herrero, J. Kong, H. S. J. van der Zant, C. Dekker, L. P. Kouwenhoven, and S. De Franceschi, Nature **434**, 484 (2005).
- <sup>45</sup> W. Hofstetter and H. Schoeller, Phys. Rev. Lett. **88**, 016803 (2002).
- <sup>46</sup> W. Hofstetter and G. Zaránd, Phys. Rev. B **69**, 235301 (2004).
- <sup>47</sup> L. Borda, G. Zaránd, W. Hofstetter, B. I. Halperin, and J. von Delft, Phys. Rev. Lett. **90**, 026602 (2003).
- <sup>48</sup> R. López, D. Sánchez, M. Lee, M.-S. Choi, P. Simon, and K. Le Hur, Phys. Rev. B **71**, 115312 (2005).
- <sup>49</sup> M. R. Galpin, D. E. Logan, and H. R. Krishnamurthy, J. Phys. C **18**, 6545 (2006).
- <sup>50</sup> M.-S. Choi, R. López, and R. Aguado, Phys. Rev. Lett. **95**, 067204 (2005).
- <sup>51</sup> W. G. van der Wiel, S. De Franceschi, J. M. Elzerman, S. Tarucha, L. P. Kouwenhoven, J. Motohisa, F. Nakajima, and T. Fukui, Phys. Rev. Lett. **88**, 126803 (2002).
- <sup>52</sup> G. Granger, M. A. Kastner, I. Radu, M. P. Hanson, and A. C. Gossard, Phys. Rev. B **72**, 165309 (2005).
- <sup>53</sup> P. G. Silvestrov and Y. Imry (2006), unpublished, cond-mat/0609355.
- <sup>54</sup> To evaluate  $R(x)$ , we have performed analytic integration of Eq. (4.35) of Ref.22.